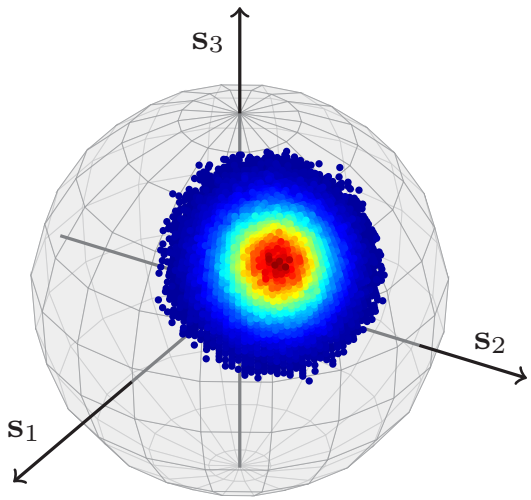

Modeling and Tracking of Stochastic Polarization Drifts in Fiber-Optic Systems

CRISTIAN B. CZEGLEDI

Department of Signals and Systems
CHALMERS UNIVERSITY OF TECHNOLOGY
Gothenburg, Sweden 2016

THESIS FOR THE DEGREE OF LICENTIATE OF ENGINEERING

Modeling and Tracking of Stochastic Polarization Drifts in Fiber-Optic Systems

Cristian B. Czegledi

CHALMERS
UNIVERSITY OF TECHNOLOGY

Communication Systems Group
Department of Signals and Systems
Chalmers University of Technology
Gothenburg, Sweden, 2016

Modeling and Tracking of Stochastic Polarization Drifts in Fiber-Optic Systems

Cristian B. Czegledi

Technical Report No. R001/2016
ISSN 1403-266X

This thesis has been prepared using LaTeX and PSTricks.

Communication Systems Group
Department of Signals and Systems
Chalmers University of Technology
SE-412 96 Gothenburg, Sweden
Phone: +46 (0)31 772 1000
www.chalmers.se

Front cover illustration:
Histogram of a random walk step over the sphere (see [Paper A] for details).

Printed by Chalmers Reproservice
Gothenburg, Sweden, February 2016

Abstract

In the past decade, accessing information has become easier than ever, leading to a rapid growth in popularity of social media, online gaming, and multimedia broadcast systems. These and other services put pressure on the Internet service providers to support high-speed Internet connections and motivate the need for faster communication systems. Fiber-optic communications are the backbone of the Internet and accommodate for this demand by evolving from the traditional intensity-modulated systems to modern coherent detection, which makes use of digital signal processing to encode the data onto multiple phase and amplitude levels of the optical carrier.

Although coherent systems enable the use of high-order modulation formats, the improved spectral efficiency comes at the cost of a reduced tolerance to impairments. These impairments are mitigated using digital signal processing algorithms, which, ideally, should be designed such that the impairments are optimally compensated in order to maximize performance. The impact of an impairment on the performance of a transmission system can be understood via a channel model, which should describe the behavior of the channel as accurately as possible. In this thesis, we consider modeling and compensation of the carrier phase noise and state of polarization drift in coherent fiber-optic systems.

A theoretical framework is introduced to model the stochastic nature of the state of polarization during transmission. The model generalizes the one-dimensional carrier phase noise random walk to higher dimensions, modeling the phase noise and state of polarization drift jointly as rotations of the optical field and it has been successfully verified using experimental data. Such a model will be increasingly important in simulating and optimizing future systems, where sophisticated digital signal processing will be natural parts. The proposed polarization drift model is the first of its kind, as prior work either models polarization drift as a deterministic process or focuses on polarization-mode dispersion in systems where the state of polarization does not affect the receiver's performance.

The typical digital signal processing solution to mitigate the phase noise and the drift of the state of polarization consists of two separate blocks that track each phenomenon independently. Such algorithms have been developed without taking into account mathematical models describing the impairments. Based on the proposed model, we study a blind tracking algorithm to compensate for these impairments. The algorithm dynamically recovers the carrier phase and state of polarization jointly for an arbitrary modulation format. Simulation results show the effectiveness of the proposed algorithm, having a fast convergence rate and an excellent tolerance to phase noise and dynamic drift of the polarization. The computational complexity of the algorithm is lower compared to state-of-the-art algorithms at similar or better performance, which makes it a strong candidate for future optical systems.

Keywords: Channel model, model-based, phase noise, phase recovery, polarization demultiplexing, polarization drift, polarization recovery.

List of Publications

This thesis is based on the following publications:

[A] C. B. Czegledi, M. Karlsson, E. Agrell, and P. Johannisson, "Polarization drift channel model for coherent fibre-optic systems," *Nature Scientific Reports*, to appear, 2016.

[B] C. B. Czegledi, E. Agrell, M. Karlsson, and P. Johannisson, "Modulation format independent joint polarization and phase tracking for optical communications," submitted to *Journal of Lightwave Technology*, Jan. 2016.

Publications by the author not included in the thesis:

[a] C. B. Czegledi, M. R. Khanzadi, and E. Agrell, "Bandlimited power-efficient signaling and pulse design for intensity modulation," *IEEE Transactions on Communications*, vol. 62, no. 9, pp. 3274–3284, Sept. 2014.

[b] C. B. Czegledi, M. R. Khanzadi, and E. Agrell, "Bandlimited power-efficient signaling for intensity modulation," in *Proc. European Conference on Optical Communication (ECOC)*, Cannes, France, Sept. 2014, p. P.3.7.

[c] C. B. Czegledi, E. Agrell, and M. Karlsson, "Symbol-by-symbol joint polarization and phase tracking in coherent receivers," in *Proc. Optical Fiber Communication Conference (OFC)*, Los Angeles, CA, Mar. 2015, p. W1E.3.

[d] M. Karlsson, C. B. Czegledi, and E. Agrell, "Coherent transmission channels as 4d rotations," in *Proc. Signal Processing in Photonic Communication (SPPCom)*, Boston, MA, Jul. 2015, p. SpM3E.2.

Acknowledgments

This thesis is not only the end result of my hours spent at the keyboard, but the product of a continuous collaboration with various people that I wish to thank.

My first big thank you goes to my supervisor Prof. Erik Agrell for his support and guidance at all levels throughout the past years. Your understanding, patience, and attention to details helped me to develop as a researcher. I am also grateful to my co-supervisor Prof. Magnus Karlsson for his patience with all my questions and misunderstandings about photonics. I feel very lucky to be supervised by you. I would also like to thank Associate Prof. Pontus Johannisson for his unlimited critical feedback pushing me to revise and improve my work.

I would like to thank my friends and colleagues at the Communication Systems group for creating an exciting work place and for the fun we had in the past years. Many thanks go to Prof. Erik Ström for his dedication in creating an inspiring research group. I would also like to thank every member of the fibre optic communications research centre (FORCE) for providing a unique and diverse research environment.

My gratitude goes to my parents who raised me with an appreciation for science and supported me in my pursuits. Last but not least, I want to thank Alexandra for her constant support and motivation.

Acronyms

4D	four-dimensional
AWGN	additive white Gaussian noise
BPS	blind phase search
CD	chromatic dispersion
CMA	constant modulus algorithm
DOF	degree of freedom
DSP	digital signal processing
MMA	multiple modulus algorithm
pdf	probability density function
PM	polarization-multiplexed
PMD	polarization-mode dispersion
QAM	quadrature-amplitude modulation
QPSK	quadrature phase-shift keying
SNR	signal-to-noise ratio
SOP	state of polarization

Contents

Part I

Overview

CHAPTER 1

Background

Communication has an important role in today's modern society and has changed the way we connect to the world. Historically, information has been conveyed through many different media ranging from cave paintings, rock-carved petroglyphs, and smoke signals to the modern communication network that we have today, known as the *Internet*. In today's digital era, it is easier than ever to access information, which lead to a rapid growth in popularity of social media, online gaming, and multimedia broadcast systems. These put pressure on the Internet service providers to support high-speed Internet connections and motivates the need for the design of faster communication systems [1].

Fiber-optic communications are the fastest form of communication technology available today and they assemble the backbone of the Internet. The optical technology transports information using light in the near-infrared spectrum over distances varying from a few meters in data-centers to thousands of kilometers over transoceanic links. The deployment of optical cables started in the 1980s when they revolutionized the communication networks and became the predominant transmission medium in telecommunication links. The first transoceanic link was installed in 1988 connecting USA and Europe [2]. The invention of optical amplifiers [3, 4] enabled wavelength-division multiplexing initiating a massive investment in system development. This technical revolution increased the data rates of commercial optical systems from approximately 1 Gb/s in the mid-1980s to 1 Tb/s by 2000 [1].

Although communication over fibers offers high data rates, historically, the employed transmission schemes utilized the spectrum rather inefficiently. As an example, the digital data was represented as the presence or absence of light, known as on–off keying. However, as the request for higher data rates increased tremendously in recent times,

this highly inefficient transmission method was replaced by more sophisticated methods that modulate the data over multiple amplitude and phase levels of the transmitted light. This has been made possible using digital signal processing (DSP) tools resulting in coherent transmission that are more robust to impairments and benefit from an improved spectral efficiency [5].

To improve the throughput even further, optical systems use two orthogonal polarizations of light to convey data. These systems are known as being polarization-multiplexed (PM) and they can double the throughput compared to a single-polarization transmission. In order to benefit from the native four-fold dimensionality of the optical field, consisting of the In-Phase and Quadrature components in two polarizations, PM transmission with four degrees of freedom (DOFs) has been constructed for optical channels [6].

PM-quadrature phase-shift keying (PM-QPSK) introduced for 100 Gb/s per channel transmission has been widely deployed and reached maturity. Recently, 200 Gb/s per channel transceivers have been made commercially available based on PM-16-quadrature-amplitude modulation (PM-16-QAM) and it is expected that in the near future, higher-order PM-M-QAM modulation formats will become a necessity for higher data rates. However, the improved spectral efficiency comes at a cost of a reduced tolerance to impairments, such as additive noise, nonlinearities, or laser phase noise. Therefore, future higher-order modulation formats require more powerful DSP that can mitigate these impairments accurately.

Before deployment into the field, newly-designed DSP algorithms must be verified and tuned. An alternative to experimental testing is numerical simulation. Simulations offer a greater flexibility than experiments and can be used to predict the behavior of a system and quantify performance. Nonetheless, simulations rely on mathematical channel models, which, in order to achieve conclusive results, should describe propagation through fibers accurately.

1.1 Thesis Organization

This thesis is a support of candidature for the licentiate degree. The licentiate degree is a predoctoral degree in the process towards the final Ph.D. degree and it is formally equivalent to half of a doctoral dissertation. The thesis documents the progress made by the candidate over a period of approximately two to two and a half years. This thesis is formatted as a collection of papers, where the first part serves as an introduction to the second part consisting of the appended papers.

The remainder of the thesis is structured as follows. Chapter 2 presents a general overview of communications over optical fibers by discussing common impairments and their mitigation. In Chapter 3, the background information for the considered mathematical representation of optical signals is introduced, and thereafter, discrete-time channel models for phase noise and polarization drift present in the literature are reviewed providing a framework for Paper A. Chapter 4 serves as background for Paper B by providing

a summary of various phase and/or polarization tracking schemes. Chapter 5 provides a short description of the appended contributions in Part II. Finally, the second part of the thesis contains the research papers.

1.2 Notation

The following notation conventions are used throughout the thesis: column vectors are denoted by bold lower case (e.g., $\mathbf{u}$) and matrices by bold upper case (e.g., $\mathbf{U}$), except a few specific cases, for literature consistency reasons, denoted by small Greek letters such as the Pauli matrices $\boldsymbol{\sigma}_i$, the basis matrices $\boldsymbol{\rho}_i$, $\boldsymbol{\lambda}_i$, and the electric field Jones vector $\mathbf{E}$. Transposition is written as $\mathbf{u}^{\mathrm{T}}$, conjugation as $\mathbf{u}^*$, and conjugate transpose as $\mathbf{u}^{\mathrm{H}}$. The $n \times n$ identity matrix is written as $\mathbf{I}_n$ and the expectation operator as $\mathbb{E}[\cdot]$. The dot operation $\boldsymbol{\alpha} \cdot \vec{\boldsymbol{\sigma}}$ should be interpreted as a linear combination of the three matrices forming the tensor $\vec{\boldsymbol{\sigma}} = (\boldsymbol{\sigma}_1, \boldsymbol{\sigma}_2, \boldsymbol{\sigma}_3)$. Multiplication of a matrix with the tensor $\vec{\boldsymbol{\sigma}}$ results in a tensor with element-wise multiplications, e.g., $\mathbf{U}\vec{\boldsymbol{\sigma}} = (\mathbf{U}\boldsymbol{\sigma}_1, \mathbf{U}\boldsymbol{\sigma}_2, \mathbf{U}\boldsymbol{\sigma}_3)$. The absolute value is denoted by $|\cdot|$ and the Euclidean norm by $\|\cdot\|$.

CHAPTER 2

Fiber-Optic Communication Systems

Fiber-optic communications rely on the total internal reflection phenomenon to guide a beam of light trough a cylindrical core made of silica glass. This core is surrounded by a cladding that confines the light into the core and whose refractive index is smaller than the one of the core. The light can propagate through the fiber in different optical modes, which are solutions to Maxwell's equations [7, Ch. 2]. Single-mode fibers support only one mode, known as the fundamental mode. This type of fiber is primarily used in long-haul coherent links covering distances larger than 1 km. Fibers with a larger core diameter than single-mode fibers allow more modes to propagate. These fibers allow the use of lower-cost electronics at the expense of increased interference levels, where the different modes have different transit times, thus leading to modal dispersion. This is called a multi-mode fiber and it is used mainly in short-range links such as access networks, consumer electronics, and within data centers.

Although optical fibers benefit from a much lower attenuation compared to the previously used copper wires, the signal still has to be amplified periodically in order to reach long transmission distances. This amplification process is not ideal and corrupts the signal with additive noise. Besides the additive noise, the transmission may suffer from various impairments, both stochastic and deterministic, which affect the transmitted data stronger as the link length increases. In this thesis, we are interested in long-haul transmission, where the data transfer is strongly affected by the channel. This chapter presents a brief description, without going into the mathematical details, of various impairments present in communications through fibers (Section 2.1), thereafter the structure of a conventional transceiver is discussed (Section 2.2).

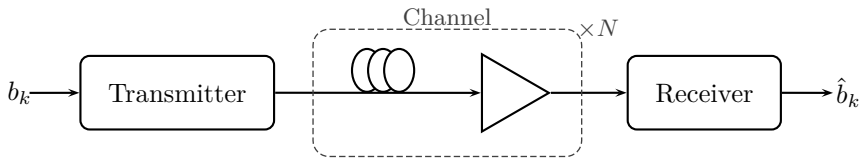

Figure 2.1: A fiber-optic link with N spans, each consisting of a fiber span and an optical amplifier.

2.1 The Fiber-Optic Channel

Fig. 2.1 shows a generic fiber-optic link. The transmitter maps the bits b_k to an optical waveform, which propagates through the channel to the receiver. The receiver outputs an estimate of the transmitted bits $\hat{b}_k$ based on the received optical waveform.

2.1.1 Signal Attenuation and Additive Noise

The optical signal attenuates as it propagates through the fiber and as the receiver requires a minimum signal power, fiber losses became a limiting factor of reaching long transmission distances. Optical fibers with practical attenuation coefficients became available in 1970s, when silica fibers were introduced [8]. These fibers have a wavelength-dependent loss spectrum, exhibiting a minimum of only 0.2 dB/km in the 1550 nm region and a secondary minimum below 0.5 dB/km around 1300 nm. These values are close to the fundamental limit of about 0.16 dB/km for silica fibers [7, Sec. 2.5.1], therefore improvements that allow transmission over thousands of kilometers were sought after by other means. Practical optical amplifiers became available in the 1990s, which allowed transmission over very long distances by periodical amplification (illustrated in Fig. 2.1) in the optical domain [3,4]. For long-haul communications, the span length is typically in the 50–120 km range, after which the signal is amplified. This setup is called lumped amplification and is widely used in current installed systems. On the other hand, distributed amplification has gained recent research interest, where the amplification is carried out throughout the entire link [9].

Optical amplifiers add noise to the transmitted signal through the generation of amplified spontaneous emission, thus degrading the signal-to-noise ratio (SNR). The accumulated noise from each span can be modeled as additive white Gaussian noise (AWGN). Fig. 2.2 shows the power profile of the signal and the accumulated noise during propagation. As can be seen, the signal suffers from attenuation in each span, after which the signal is amplified, thus increasing the noise level.

2.1.2 Phase Noise

Coherent systems benefit from an improved spectral efficiency by modulating the phase and the amplitude of the optical field, in both polarizations. In order to have access to

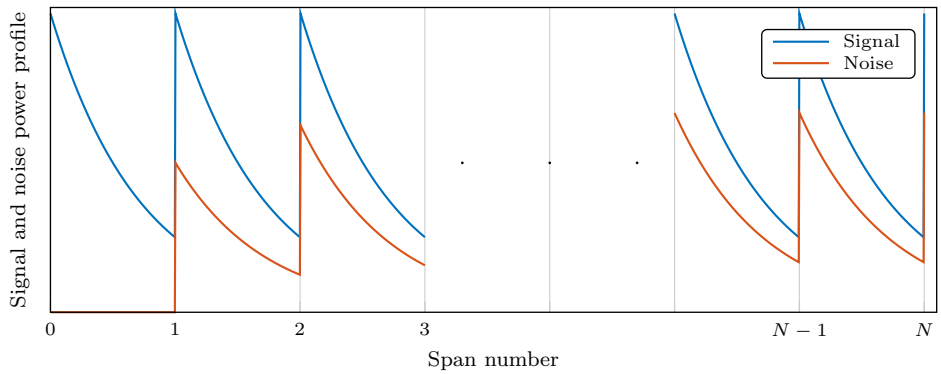

Figure 2.2: The power profile of the signal and noise as a function of span number is shown.

both phase and amplitude, coherent systems rely on two independent lasers, one at the transmitter and one at the receiver. The optical carrier wave produced by the transmitter laser is modulated and then coupled to the optical fiber. The receiver laser, often called local oscillator, serves as a reference and it is combined with the incoming optical field. The frequencies of the transmitter laser and local oscillator can be chosen to be the same or different resulting in two different detection techniques. They are known as homodyne and heterodyne receivers, respectively [10]. In the case of heterodyne detection, the incoming optical signal is first down-converted from the carrier frequency (191–195 THz) to an intermediate frequency ($\sim$1 GHz) and then processed electronically. On the other hand, in the case of homodyne detection, the intermediate frequency is (ideally) zero.

The local oscillator and the transmitter laser are not synchronized and have phase fluctuations, resulting in phase noise, thus creating the need for carrier-phase synchronization. Heterodyne and homodyne architectures require a demanding optical loop synchronization circuit to phase lock the local oscillator, where the latter approach is more phase sensitive than the former at the advantage of a 3 dB improved SNR [10]. Intradyne detection [11] is an architecture that down-converts the incoming optical signal to a frequency that should be smaller (or ideally zero) than the symbol rate with typical values in the range 0–5 GHz [12]. Compared to heterodyne or homodyne, the intradyne detection has the advantage of not requiring an optical phase-locked loop and compensates for the phase noise electronically.

Ideally, the spectral shape of a laser is a delta function at the carrier frequency. However, practical lasers have a broader spectrum, which is the source of the phase noise [13]. The phase noise of an optical link can be quantified by the linewidth sum $\Delta\nu$ of the transmitter and receiver lasers in relation to the symbol period T. The laser linewidth relates to the inverse of the coherence time of a laser, which is a measure to characterize the time duration over which the laser is stable. The coherence time is desired to be much larger than the symbol period, and often the phase-noise sensitivity of a system is quantified

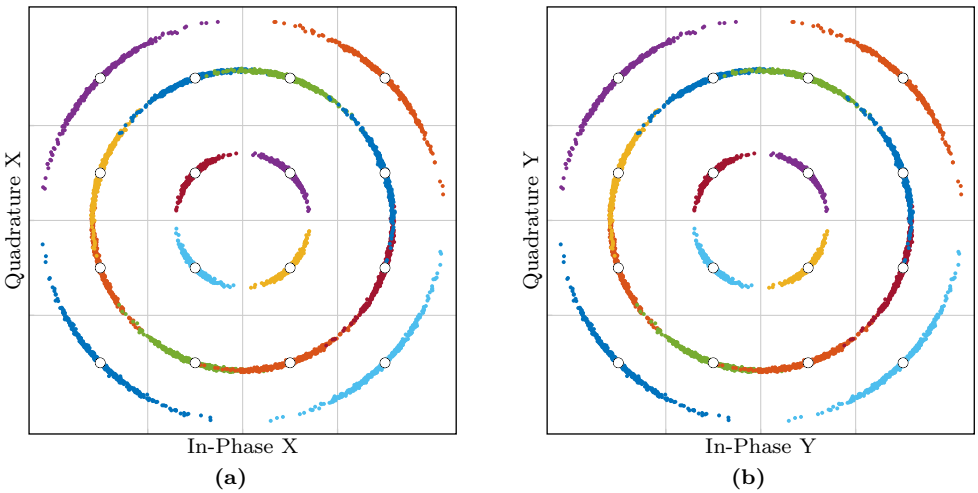

Figure 2.3: PM-16-QAM constellation affected by phase noise. Both X (a) and Y (b) polarizations are affected by the same rotation. The grid lines represent the Voronoi regions of a detector designed for AWGN, which, in this case, will lead to catastrophic errors.

by the dimensionless measure $\Delta\nu T$.

Phase noise leads to a random rotation of the received PM constellation with a common angle in both polarizations. This random rotation induces catastrophic errors in phase-modulated transmission if it is not compensated for. Fig. 2.3 shows the effect of phase noise on a PM-16-QAM constellation. Phase noise is further discussed in Chapters 3 and 4, where modeling and different compensation techniques are reviewed.

2.1.3 Polarization State Drift

Light is an oscillating electromagnetic field, whose propagation can be described, similarly to radio waves, via a sinusoidal wave of the electric field. The orientation of the oscillation of this field is called polarization. The simplest type is linear polarization, where the field is confined to oscillate only in a single fixed plane. Fig. 2.4a shows an example of a linearly polarized lightwave, whose electromagnetic wave E oscillates in the $-45°$ plane. The E field can be decomposed into two orthogonal components, commonly referred as E_x and E_y. In the example shown in Fig. 2.4a, the E_x and E_y components are sinusoidals of the same amplitude and phase. Combinations of E_x and E_y that do not have the same phase or/and amplitude will result in different behavior of the total field E. In some of these cases, the field E will not oscillate in a single plane, but will rotate at the optical frequency. Fig. 2.4b illustrates the case called circular polarization where E_x and E_y have the same amplitude but a $\pi/2$ phase difference, thus the wave E will describe a circle

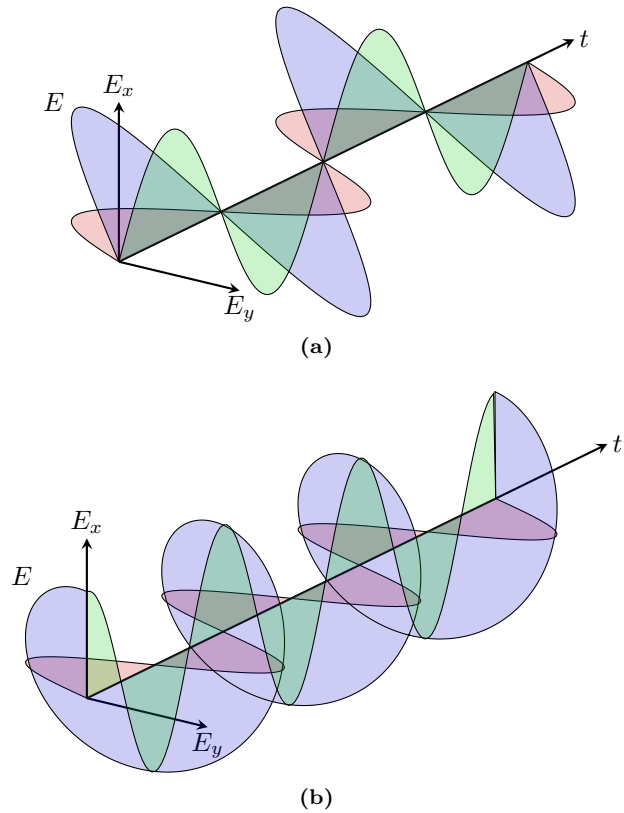

Figure 2.4: The E_x (green) and E_y (red) components of the electromagnetic field as a function of time t, which combine and form the aggregate field E (blue). In the figure on top, linear polarization is shown where the field E oscillates in the $-45°$ plane, whereas the bottom figure shows circular polarization (obtained by shifting E_x by $\pi/2$) where the field E describes a circle as time progresses.

as time progresses. These different polarizations of light are called *states of polarization* (SOPs). The SOP of light can be fully described by three DOFs corresponding to the amplitudes of the E_x and E_y components and the relative phase difference between them.

Coherent fiber-optic communications make use of the orthogonality between the E_x and E_y components, so called the X and Y polarizations, which can be independently modulated in phase and amplitude and then detected at the receiver. Ideally, light propagating through a straight fiber will preserve the SOP in which it was launched. However, this is not the case for real fibers, which are bent. These bends break the orthogonality between E_x and E_y resulting in a power exchange between the four components of the optical field, which is called *SOP drift*. The geometry of fibers varies both along the fiber and in time due to the diversity of the environment passed by the cables and

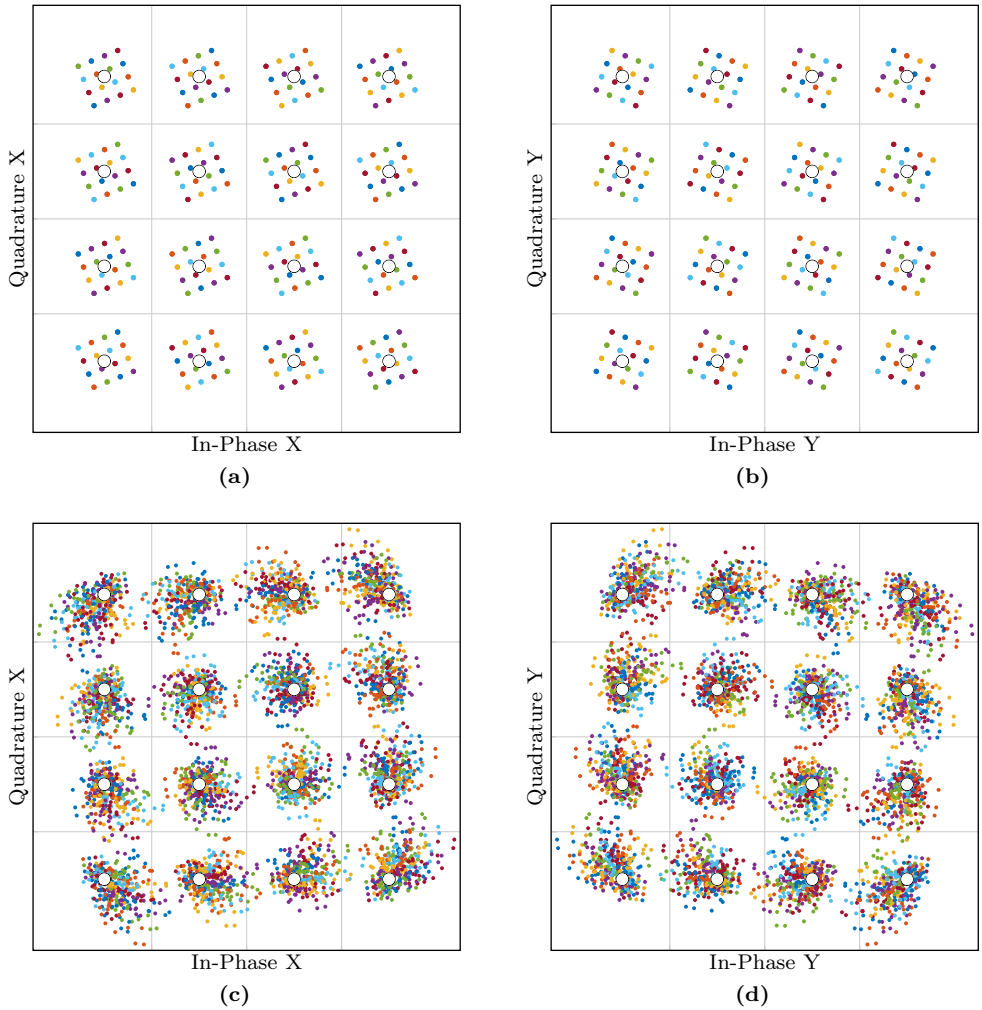

Figure 2.5: PM-16-QAM constellation affected by SOP drift. PM-16-QAM consists of 256 points obtained by all possible combinations between the X and Y polarization. Different colors represent the 16 possible combinations of a point with the complement polarization. The first row illustrates the effect of a static SOP rotation, where each point is split into 16 points. In the second row, the effects of a dynamic SOP drift are shown, where different points of the same color represent different time instances. The grid lines represent the Voronoi regions of a detector designed for AWGN, which, in this case, will lead to catastrophic errors.

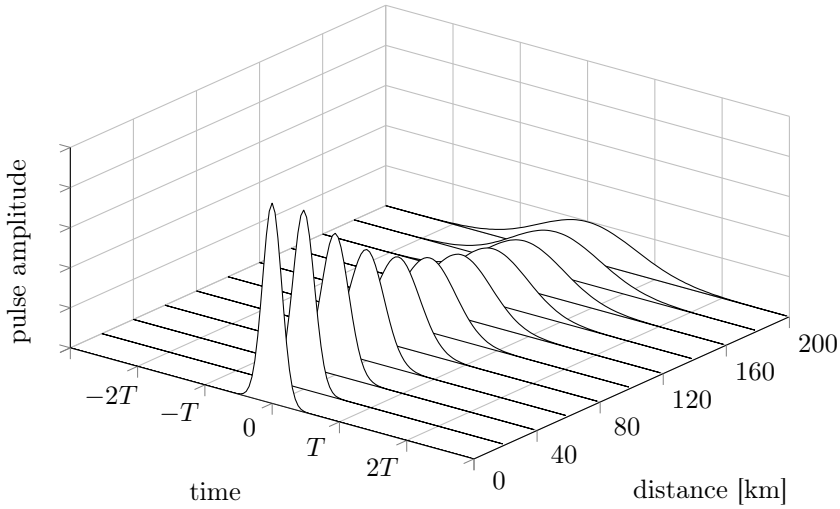

Figure 2.6: The evolution in the time domain of a pulse affected by CD. The pulse broadens as it propagates, thus causing interference to the neighboring pulses.

temperature/mechanical changes, thus the drift of the SOP is considered to be *random*.

The SOP drift can be seen as a four-dimensional (4D) rotation of the 4D PM constellation, and it is illustrated in Fig. 2.5. In order to successfully convey data through such a channel, a synchronization block is required to undo these effects. The fact that the drift is stochastic restricts the compensation to be done at the receiver since the behavior of the phenomenon depends on the fiber and cannot be perfectly predicted. Different approaches on how to model mathematically SOP drifts are discussed in Chapter 3, whereas compensation techniques are examined in Chapter 4.

2.1.4 Chromatic Dispersion

In a communication system, the waveform generated by the transmitter, which is then launched into the fiber, spreads over different frequencies/wavelengths. These different frequency components travel through the optical fiber at different speed causing pulse broadening in the time domain [14, Sec. 1.2.3], a phenomenon called *chromatic dispersion* (CD). In other words, different spectral components launched into the fiber at the same time have different transit times and arrive at the receiver at different times. This can be seen as an all-pass filter that causes a frequency-dependent phase shift in the frequency domain without changing the amplitude of the spectrum.

The time of arrival difference between the fast and slow spectral components, i.e., the pulse broadening, depends on the length of the link and on the dispersion parameter, which is specific for each fiber. In principle, CD is a deterministic effect and can be fully compensated for if the length of the transmission and the dispersion parameter are

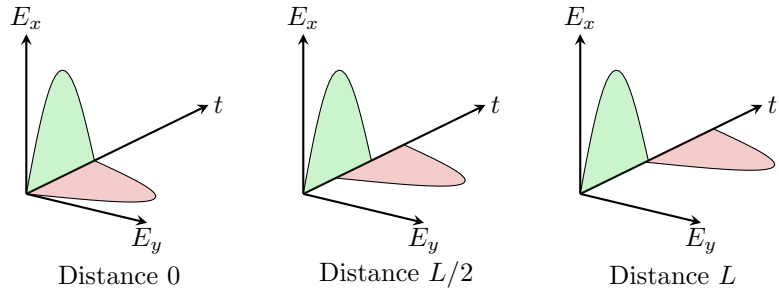

Figure 2.7: Example of PMD effects in the time domain, where two pulses with equal power in the X and Y polarizations propagate through a short fiber of length L. The pulses are shown at three different propagated distances and the time separation between them increases with the distance.

known. Traditionally, CD has been compensated for in the optical domain by inserting a dispersion-compensating fiber [14, Sec. 1.2.3] or a fiber Bragg grating [15] in each span compensating for the accumulated dispersion in that span. Recently, digital compensation attracted attention in the form of a DSP block at the receiver/transmitter that compensates/precompensates for the entire link at once [16].

Fig. 2.6 illustrates the evolution in the time domain of a pulse affected by CD. It should be noted that both polarizations are affected identically by CD regardless of the SOP.

2.1.5 Polarization Mode Dispersion

Practical fibers exhibit imperfections in their shape of the core along the fiber due to the manufacturing process and due to the applied mechanical/thermal stress during and after installation. These imperfections break the cylindrical symmetry of the fiber, leading to a phenomenon called *birefringence*. Birefringence causes dispersion, where the two orthogonal polarizations, which normally travel at the same speed, travel at different speed. This phenomenon is called *polarization-mode dispersion* (PMD) [17]. Fig. 2.7 shows the effect of PMD in the time domain on two pulses launched with equal power in the two orthogonal polarizations. During propagation, the two pulses have different velocities acquiring a time separation between them, which is called *differential group delay*. For simplicity, in this example the delay occurred between the X and Y axes, which is not always the case. The delay can occur between any pair of orthogonal axes, called *birefringence axes*.

Similarly to CD, this effect is deterministic for short fibers as the differential group delay grows linearly with the fiber length. However, this is not the case for long fibers where PMD is no longer additive. The birefringence axes have a random orientation along the fiber and their orientation changes randomly with time. The acquired PMD during transmission highly depends on the installation details of the fiber, such as bends,

thermal variations, etc., therefore PMD behaves differently on a fiber spool than on a deployed fiber.

2.2 Coherent Transmission

Coherent transmission was developed as a necessity to improve the spectral efficiency and sensitivity of the traditional direct-detection transmission [5, 18]. The latter uses on–off keying, which is detected at the receiver using a photodiode [19–21]. This photodiode generates an electric current proportional to the received optical power ignoring the phase of the signal. The invention of the coherent transmitter and receiver, together with DSP advances, enabled the use of spectrally-efficient modulation formats and compensation of distortions in the digital domain.

2.2.1 Transmitter

The common solution to modulate the coherent optical signal is based on Mach–Zehnder modulators, which independently modulate each dimension of the optical field. Fig. 2.8 shows an overview schematic of a coherent transmitter [22]. A coherent light source, such as a laser, is split into two arms by a polarization beam splitter. Each arm corresponds to the X and Y polarization. Thereafter, each arm is again split into two arms, corresponding to the In-Phase and Quadradure components. Each arm is modulated by a Mach–Zehnder modulator, and then recombined after a $\pi/2$-phase shift has been applied to one of the arms, thus forming the phase- and amplitude-modulated signal. To one of the two such phase- and amplitude-modulated signals a polarization rotation is applied such that it becomes Y-polarized from X-polarized. Finally, the two X- and Y-polarized signals are recombined by a polarization beam combiner and then launched into the fiber.

2.2.2 Receiver

A simplified schematic[1] of a coherent receiver and the flow from the optical signal to data are illustrated in Fig. 2.9 [23]. The shown blocks mitigate the impairments discussed in the earlier sections.

- Optical front end. This block linearly maps the received optical field to electric signals, which are then sampled using analog-to-digital converters to obtain the corresponding digital signals. The incoming optical signal is mixed with the local oscillator using two 90° hybrids [24, Sec. 3.1.3], one for each polarization, and four electric signals are output corresponding to the two quadratures in the two polarizations. Phase noise, discussed in Section 2.1.2, as well as a frequency offset,

[1] Several blocks, such as the analog-to-digital conversion, de-skew and orthonormalization, are skipped since they are not relevant to this thesis.

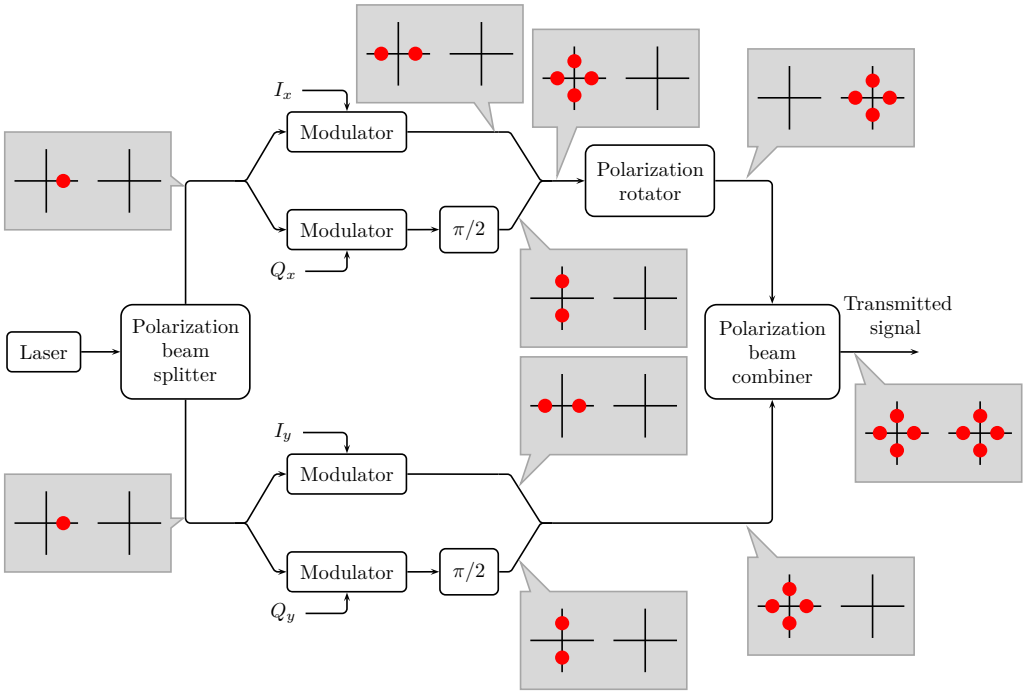

Figure 2.8: Schematic of an optical coherent transmitter [22]. The shown constellations exemplify the generation of PM-QPSK, where the left (right) side corresponds to the X (Y) polarization.

are generated at this stage as a result of the phase and frequency difference between the transmitter laser and the local oscillator.

- CD compensation. This is a static equalization stage usually realized with finite-impulse response filters [23], although infinite-impulse response filters are also an option [25]. Two identical filters are used independently for the two polarizations, typically implemented in the frequency domain due to a more efficient implementation. However, is has been shown that time-domain implementations are more power-efficient for short-haul links [26, 27]. At this stage, matched filtering can be applied by convolving the filters with the desired pulse shape [23] and, for long distances, compensation of nonlinear transmission effects can be employed [28, 29].

- PMD compensation and SOP tracking. This block compensates for time-varying impairments using a bank of finite-impulse response filters in the time domain. These filters have a shorter impulse response than the ones described above, and are dynamically updated such that they adapt to the varying channel. The update

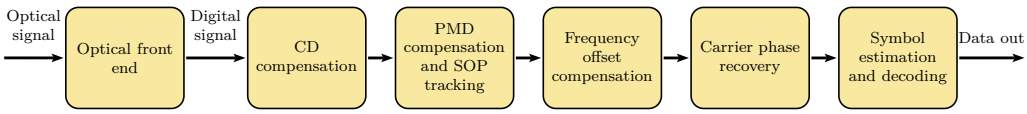

Figure 2.9: Simplified schematic of a coherent receiver.

of the filters is often done in the Jones space using the constant modulus algorithm (CMA) or the multiple modulus algorithm (MMA) (discussed in Chapter 4) or in the Stokes space [30, 31].

- Frequency offset compensation. The compensation for residual carrier frequency can be done in the time domain using fourth-order methods that take advantage of the four-fold rotational symmetry of PM-QAM constellations [32]. Nevertheless, methods in the frequency domain have been proposed [33], which center the peak of the spectrum around the zero frequency.

- Carrier phase recovery. Similar to frequency estimation, the carrier phase can be estimated using fourth-order methods [34] or methods that scan over a set of possible test phases in order to minimize an error function [35]. Blind algorithms, which do not know the transmitted data, suffer from the four-fold ambiguity of PM-QAM constellations. In order to resolve this issue, and also minimize the impact of cycle slips, differential coding [24, Sec. 2.6.1] is employed, which induces an increased bit error rate. On the other hand, data-aided algorithms do not require differential coding, but reduce the spectral efficiency by inserting pilots. Phase-noise compensation techniques are examined in Chapter 4.

- Symbol detection and decoding. At this stage, the signal is ready to be decoded into bits. Forward error correction is applied using either soft-decision or hard-decision decoding [36]. The latter is more common due to its lower complexity at the cost of lower performance, but soft decision has gained more interest recently [37].

The description above considers impairment-compensation only at the receiver. However, DSP can be applied also at the transmitter in order to optimize the overall performance. Moreover, future receivers may combine different DSP blocks in order to improve performance [38].

CHAPTER 3

Discrete-Time Channel Models

A channel model is an analytical description of the signal propagation through a medium relating the output to the input. This model can include, besides the impairments that arise in the propagation medium, elements of the transmitter and receiver. Channel models can be used in simulations to test and verify transmission schemes and their accompanying DSP. In general, simulations offer a greater flexibility than experiments and can be used to predict the behavior of a system before setting up time-consuming experiments.

This thesis is concerned with phase noise and drift of the SOP, and this chapter describes mathematically the propagation of the electromagnetic field in the presence of these impairments. Section 3.1 reviews the mathematical tools used to model optical signals, Section 3.2 describes phase-noise modeling, whereas Section 3.3 serves as the motivation for Paper A to develop a channel model for SOP drift.

3.1 Vector Representation of Optical Signals

In this section, different possibilities of representing optical signals and their propagation is described. First, the Jones formalism is described, followed by the 4D formalism, thereafter the Stokes formalism is presented.

3.1.1 Jones Description

The coherent optical signal has two quadratures in two polarizations and can be described using a complex-valued two-dimensional vector, the so-called *Jones vector*, as a function

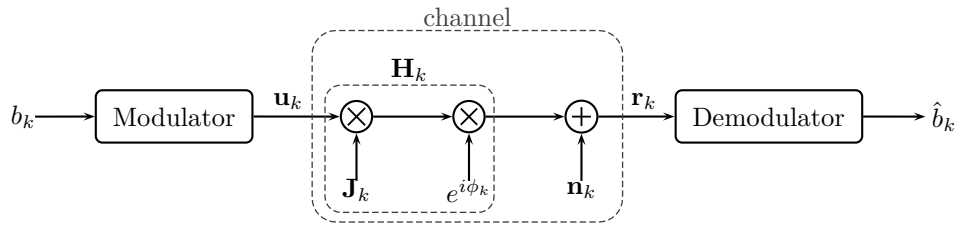

Figure 3.1: Block diagram of a system considering a transmitter, channel, and a receiver. The channel consists of phase noise, SOP drift, and AWGN.

of distance z and time t

$$\mathbf{E}(z,t) = \begin{pmatrix} E_x(z,t) \\ E_y(z,t) \end{pmatrix}, \tag{3.1}$$

where E_x and E_y are complex-baseband signals denoting the X and Y field components. Each component combines the In-Phase and Quadrature as the real and imaginary parts.

The transmitted signal $\mathbf{E}(0,t)$ into the transmission medium is obtained by linearly modulating the information symbols $\mathbf{u}_k \in \mathbb{C}^2$

$$\mathbf{E}(0,t) = \sum_k \mathbf{u}_k p(t - kT), \tag{3.2}$$

using a real-valued pulse shape $p(t)$, where T is the symbol (baud) interval. The discrete transmitted symbols $\mathbf{u}_k$ are drawn independently from a finite constellation $\mathscr{C} = \{\mathbf{c}_1, \mathbf{c}_2, ..., \mathbf{c}_M\}$ with equal probability. The average energy per symbol is the average of $\|\mathbf{u}_k\|^2$ and in this case equals

$$E_s = \frac{1}{M} \sum_{k=1}^{M} \|\mathbf{c}_k\|^2. \tag{3.3}$$

The received discrete symbols at distance L are obtained from the received electric field $\mathbf{E}(L,t)$ as

$$\mathbf{r}_k = \int_{-\infty}^{\infty} \mathbf{E}(L,t) p(t - kT) \mathrm{d}t, \tag{3.4}$$

by matched filtering and sampling.

Assuming that the CD has been successfully compensated for and polarization-dependent losses and PMD are negligible, the propagation of the symbols $\mathbf{u}_k$ in the presence of phase noise, SOP drift, and AWGN can be described as

$$\mathbf{r}_k = \mathbf{H}_k \mathbf{u}_k + \mathbf{n}_k, \tag{3.5}$$

where $\mathbf{H}_k \in \mathbb{C}^{2\times 2}$ is a unitary matrix, the so-called *Jones matrix*, which preserves the input power during propagation and models the phase-noise and SOP-drift effects, and

$\mathbf{n}_k \in \mathbb{C}^2$ denotes the additive noise represented by two independent complex circular zero-mean Gaussian random variables with variance $N_0/2$ per real dimension, i.e., $\mathbb{E}[\mathbf{n}_k \mathbf{n}_k^{\mathrm{H}}] = N_0 \mathbf{I}_2$ [6]. Fig. 3.1 shows a block diagram of the model described above. This model is a 2×2 multiple-input multiple-output system, where the inputs and outputs are the two different polarizations of light. Such multiple-input multiple-output schemes are widely deployed in communication over radio frequencies, where multiple inputs and outputs are achieved by using different antennas [39].

The matrix $\mathbf{H}_k$ belongs to the unitary group of degree two, denoted by $U(2)$, such that

$$\mathbf{H}_k^{\mathrm{H}} \mathbf{H}_k = \mathbf{H}_k \mathbf{H}_k^{\mathrm{H}} = \mathbf{I}_2, \tag{3.6}$$

$$|\det \mathbf{H}_k| = 1. \tag{3.7}$$

In general, complex 2×2 matrices have eight DOFs, i.e., the real and imaginary parts of the four elements, whereas the matrices in $U(2)$, after applying (3.6), have only *four* DOFs[1]. Such matrices can be expressed by the matrix function $H(\phi, \boldsymbol{\alpha})$ using the *matrix exponential* parameterized by four variables ϕ modeling the phase noise, and $\boldsymbol{\alpha} = (\alpha_1, \alpha_2, \alpha_3)$ modeling the SOP drift, according to [40, 41]

$$H(\phi, \boldsymbol{\alpha}) = \exp(-i(\boldsymbol{\alpha} \cdot \vec{\boldsymbol{\sigma}} + \phi \mathbf{I}_2)), \tag{3.8}$$

where $i = \sqrt{-1}$ and $\vec{\boldsymbol{\sigma}} = (\boldsymbol{\sigma}_1, \boldsymbol{\sigma}_2, \boldsymbol{\sigma}_3)$ is a tensor of the Pauli spin matrices [41]

$$\boldsymbol{\sigma}_1 = \begin{pmatrix} 1 & 0 \\ 0 & -1 \end{pmatrix}, \qquad \boldsymbol{\sigma}_2 = \begin{pmatrix} 0 & 1 \\ 1 & 0 \end{pmatrix}, \qquad \boldsymbol{\sigma}_3 = \begin{pmatrix} 0 & -i \\ i & 0 \end{pmatrix}. \tag{3.9}$$

This notation of $\boldsymbol{\sigma}_i$ complies with the definition of the Stokes vector (3.36), and it is different from the notation introduced by Frigo [40]. The vector $\boldsymbol{\alpha}$ can be expressed as a product $\boldsymbol{\alpha} = \theta \mathbf{a}$ of its length $\theta = \|\boldsymbol{\alpha}\|$ in the interval $[0, \pi)$ and the unit vector $\mathbf{a} = (a_1, a_2, a_3)$, which represents its direction on the unit sphere.

The Pauli matrices are commonly used in the polarization literature and in addition to the three matrices stated above, the identity matrix is often denoted by $\boldsymbol{\sigma}_0$. These matrices are Hermitian and have zero trace, except $\boldsymbol{\sigma}_0$. They also satisfy the identities

$$\boldsymbol{\sigma}_0 = \boldsymbol{\sigma}_i^2 \tag{3.10}$$

for $i = 1, 2, 3$, and

$$\boldsymbol{\sigma}_1 \boldsymbol{\sigma}_2 = -\boldsymbol{\sigma}_2 \boldsymbol{\sigma}_1 = i \boldsymbol{\sigma}_3. \tag{3.11}$$

The Pauli matrices are linearly independent, therefore any complex 2×2 matrix can be written as

$$\mathbf{C} = \sum_{k=0}^{3} c_k \boldsymbol{\sigma}_k, \tag{3.12}$$

[1] Note that the constraint (3.7) is already covered by (3.6), therefore it does not reduce the DOFs.

where $c_k \in \mathbb{C}$ and can be calculated as

$$c_k = \frac{\mathrm{Tr}(\mathbf{C}\boldsymbol{\sigma}_k)}{2}. \tag{3.13}$$

The matrix exponential in (3.8) is defined as [42, p. 165]

$$\exp \mathbf{A} = \sum_{k=0}^{\infty} \frac{1}{k!}\mathbf{A}^k \tag{3.14}$$

for any $\mathbf{A} \in \mathbb{C}^{n\times n}$.

The two phenomena modeled by $\mathbf{H}_k$ in (3.5) can be separated by factoring[2] out the phase noise ϕ from (3.8) such that

$$H(\phi, \boldsymbol{\alpha}) = e^{-i\phi} J(\boldsymbol{\alpha}), \tag{3.15}$$

where

$$J(\boldsymbol{\alpha}) = \exp(-i\boldsymbol{\alpha} \cdot \vec{\boldsymbol{\sigma}}) \tag{3.16}$$

strictly models the SOP drift. In this case, (3.5) can be rewritten as

$$\mathbf{r}_k = e^{-i\phi_k} \mathbf{J}_k \mathbf{u}_k + \mathbf{n}_k, \tag{3.17}$$

where the matrix $\mathbf{J}_k$ is a unitary matrix that belongs to the special unitary group of degree two, denoted by $SU(2)$, and can be described by the matrix function $J(\boldsymbol{\alpha})$. This group of matrices is a subgroup of $U(2)$ and satisfies

$$\det \mathbf{J}_k = 1, \tag{3.18}$$

opposed to (3.7). The constraint (3.18) reduces the DOFs of such matrices to only *three*, i.e., the elements of $\boldsymbol{\alpha}$.

The functions $H(\phi, \boldsymbol{\alpha})$ and $J(\boldsymbol{\alpha})$ can be rewritten after expanding (3.8) and (3.16) into the Taylor series (3.14) and using $(\boldsymbol{\alpha} \cdot \vec{\boldsymbol{\sigma}})^2 = \theta^2 \mathbf{I}_2$ as

$$H(\phi, \boldsymbol{\alpha}) = e^{-i\phi}(\mathbf{I}_2 \cos\theta - i\mathbf{a} \cdot \vec{\boldsymbol{\sigma}} \sin\theta), \tag{3.19}$$

$$J(\boldsymbol{\alpha}) = \mathbf{I}_2 \cos\theta - i\mathbf{a} \cdot \vec{\boldsymbol{\sigma}} \sin\theta. \tag{3.20}$$

Since $\mathbf{H}_k$ and $\mathbf{J}_k$ are unitary, their inverses can be found by the conjugate transpose operation or by negating ϕ and $\boldsymbol{\alpha}$, since

$$H(\phi, \boldsymbol{\alpha})^{-1} = H(\phi, \boldsymbol{\alpha})^{\mathrm{H}} = H(-\phi, -\boldsymbol{\alpha}), \tag{3.21}$$

$$J(\boldsymbol{\alpha})^{-1} = J(\boldsymbol{\alpha})^{\mathrm{H}} = J(-\boldsymbol{\alpha}). \tag{3.22}$$

[2] This factorization is possible only for $\phi\mathbf{I}_2$ since $\exp(\mathbf{X}+\mathbf{Y}) = \exp\mathbf{X}\exp\mathbf{Y} = \exp\mathbf{Y}\exp\mathbf{X}$ holds only if $\mathbf{XY} = \mathbf{YX}$ for any $\mathbf{X}, \mathbf{Y} \in \mathbb{C}^{n\times n}$.

3.1.2 4D Real Description

In the 4D formalism, the Jones vectors are represented using 4D real vectors defined as

$$\mathbf{v}_{\mathbf{z}} = \begin{pmatrix} \mathcal{R}e(z_1) \\ Im(z_1) \\ \mathcal{R}e(z_2) \\ Im(z_2) \end{pmatrix}, \tag{3.23}$$

for any $\mathbf{z} = [z_1, z_2]^{\mathrm{T}} \in \mathbb{C}^2$. The analogue to the propagation model (3.5) of the optical field is described by [43–45]

$$\mathbf{v}_{\mathbf{r}_k} = \mathbf{R}_k \mathbf{v}_{\mathbf{u}_k} + \mathbf{v}_{\mathbf{n}_k}, \tag{3.24}$$

where $\mathbf{v}_{\mathbf{u}_k}$ ($\mathbf{v}_{\mathbf{r}_k}$) is the transmitted (received) symbol, $\mathbf{v}_{\mathbf{n}_k}$ is the additive noise, and $\mathbf{R}_k$ is a 4×4 real orthogonal matrix (equivalent of $\mathbf{H}_k$) modeling both the phase noise and the SOP drift such that

$$\mathbf{v}_{\mathbf{H}_k \mathbf{u}_k} = \mathbf{R}_k \mathbf{v}_{\mathbf{u}_k}, \tag{3.25}$$

where $\mathbf{v}_{\mathbf{H}_k \mathbf{u}_k}$ is obtained by applying (3.23) to $\mathbf{H}_k \mathbf{u}_k$.

The matrix $\mathbf{R}_k$ belongs to the special orthogonal group of 4×4 matrices, denoted by $SO(4)$, and satisfies

$$\mathbf{R}_k^{\mathrm{T}} \mathbf{R}_k = \mathbf{R}_k \mathbf{R}_k^{\mathrm{T}} = \mathbf{I}_4, \tag{3.26}$$

$$\det \mathbf{R}_k = 1. \tag{3.27}$$

This group is also called the rotation group since it consists of all possible 4D rotation matrices and is a subset of the orthogonal group, where the determinant can be either 1 or -1.

After constraining any real 4×4 matrix with 16 DOFs to satisfy (3.26) and (3.27), it can be shown that a matrix $\mathbf{R}_k$ that belongs to $SO(4)$ has *six* DOFs. Therefore, 4×4 real orthogonal matrices $\mathbf{R}_k$ are able to span over a richer space than the Jones matrices $\mathbf{H}_k$ can (four DOFs). Jones matrices can model all physically realizable phenomena of wave propagation and the extra two DOFs of $\mathbf{R}_k$ are not possible for photon propagation [43].

The matrix $\mathbf{R}_k$ can be expressed using the matrix function [43]

$$R(\phi, \boldsymbol{\alpha}) = \exp((\phi, 0, 0) \cdot \vec{\boldsymbol{\lambda}} - \boldsymbol{\alpha} \cdot \vec{\boldsymbol{\rho}}), \tag{3.28}$$

$$= (\mathbf{I}_4 \cos\phi - \boldsymbol{\lambda}_1 \sin\phi)(\mathbf{I}_4 \cos\theta - \mathbf{a} \cdot \vec{\boldsymbol{\rho}} \sin\theta), \tag{3.29}$$

and its inverse is

$$R(\phi, \boldsymbol{\alpha})^{-1} = R(\phi, \boldsymbol{\alpha})^{\mathrm{T}} = R(-\phi, -\boldsymbol{\alpha}). \tag{3.30}$$

The matrices $\vec{\boldsymbol{\rho}} = (\boldsymbol{\rho}_1, \boldsymbol{\rho}_2, \boldsymbol{\rho}_3)$, $\vec{\boldsymbol{\lambda}} = (\boldsymbol{\lambda}_1, \boldsymbol{\lambda}_2, \boldsymbol{\lambda}_3)$ [43, eqs. (20)–(25)]

$$\boldsymbol{\rho}_1 = \begin{pmatrix} 0 & -1 & 0 & 0 \\ 1 & 0 & 0 & 0 \\ 0 & 0 & 0 & 1 \\ 0 & 0 & -1 & 0 \end{pmatrix}, \ \boldsymbol{\rho}_2 = \begin{pmatrix} 0 & 0 & 0 & -1 \\ 0 & 0 & 1 & 0 \\ 0 & -1 & 0 & 0 \\ 1 & 0 & 0 & 0 \end{pmatrix}, \ \boldsymbol{\rho}_3 = \begin{pmatrix} 0 & 0 & 1 & 0 \\ 0 & 0 & 0 & 1 \\ -1 & 0 & 0 & 0 \\ 0 & -1 & 0 & 0 \end{pmatrix}, \quad (3.31)$$

$$\boldsymbol{\lambda}_1 = \begin{pmatrix} 0 & 1 & 0 & 0 \\ -1 & 0 & 0 & 0 \\ 0 & 0 & 0 & 1 \\ 0 & 0 & -1 & 0 \end{pmatrix}, \ \boldsymbol{\lambda}_2 = \begin{pmatrix} 0 & 0 & 0 & -1 \\ 0 & 0 & -1 & 0 \\ 0 & 1 & 0 & 0 \\ 1 & 0 & 0 & 0 \end{pmatrix}, \ \boldsymbol{\lambda}_3 = \begin{pmatrix} 0 & 0 & 1 & 0 \\ 0 & 0 & 0 & -1 \\ -1 & 0 & 0 & 0 \\ 0 & 1 & 0 & 0 \end{pmatrix}, \quad (3.32)$$

are six constant matrices that form the basis for any 4D skew-symmetric real matrix and satisfy [43]

$$\boldsymbol{\rho}_i^2 = \boldsymbol{\lambda}_i^2 = -\mathbf{I}_4 \text{ for } i = 1, 2, 3, \quad (3.33)$$

$$\boldsymbol{\rho}_1\boldsymbol{\rho}_2\boldsymbol{\rho}_3 = -\boldsymbol{\rho}_2\boldsymbol{\rho}_1\boldsymbol{\rho}_3 = \mathbf{I}_4, \quad (3.34)$$

$$\boldsymbol{\rho}_1\boldsymbol{\rho}_2\boldsymbol{\rho}_3 = -\boldsymbol{\lambda}_2\boldsymbol{\lambda}_1\boldsymbol{\lambda}_3 = \mathbf{I}_4. \quad (3.35)$$

Note that in (3.28), two DOFs modeled by the scalars corresponding to $\boldsymbol{\lambda}_2, \boldsymbol{\lambda}_3$ are shown for pedagogical reasons, but have been deliberately set to zero such that a one-to-one mapping between Jones matrices $\mathbf{H}_k$ and real 4×4 matrices $\mathbf{R}_k$ is possible. However, any 4D real rotation matrix belonging to $SO(4)$ can be expressed using (3.28) by parameterizing all six DOFs.

3.1.3 Stokes Description

Another option for vector representation of optical signals is using Stokes vectors [46]. In general, Stokes vectors are 4D, but for fully polarized light and no polarization dependent losses (which is the case for this thesis), the Stokes vectors can be reduced to be three-dimensional. In this case, the equivalent Stokes vector of a Jones vector $\mathbf{z}$ is [47, eq. (2.5.26)]

$$\mathbf{s}_\mathbf{z} = \mathbf{z}^\mathrm{H}\vec{\boldsymbol{\sigma}}\mathbf{z} = \begin{pmatrix} |z_1|^2 - |z_2|^2 \\ 2\mathcal{Re}(z_1 z_2^*) \\ -2\mathit{Im}(z_1 z_2^*) \end{pmatrix}, \quad (3.36)$$

for any $\mathbf{z} = [z_1, z_2]^\mathrm{T} \in \mathbb{C}^2$, where the ith component of $\mathbf{s}_\mathbf{z}$ is given by $\mathbf{z}^\mathrm{H}\boldsymbol{\sigma}_i\mathbf{z}$. The absent fourth component is the optical power $\mathbf{z}^\mathrm{H}\mathbf{z}$. In can be noted from (3.36) that applying a common phase rotation to both z_1 and z_2 will not change $\mathbf{s}_\mathbf{z}$. E.g., both

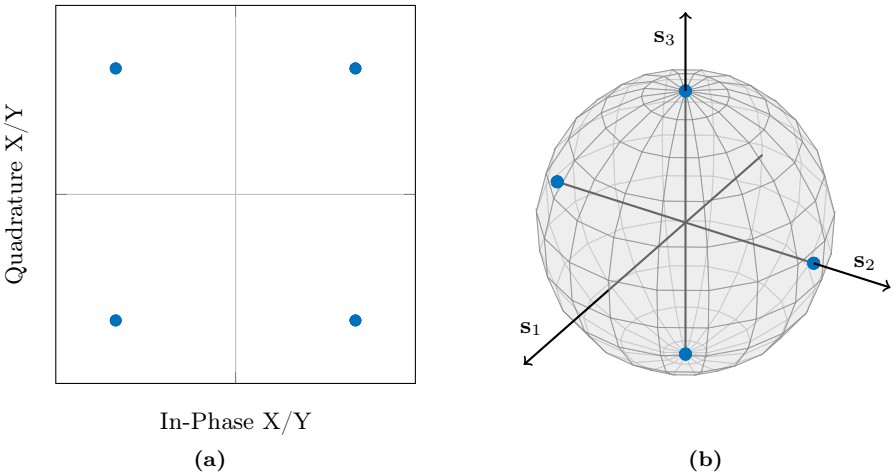

Figure 3.2: PM-QPSK constellation shown in the Jones/4D space (a) and Stokes space (b).

$\mathbf{z}_1 = [1+i, 1+i]^{\mathrm{T}}$ and $\mathbf{z}_2 = [-1-i, -1-i]^{\mathrm{T}}$ will result in $\mathbf{s}_{\mathbf{z}} = [0, 4, 0]^{\mathrm{T}}$, where a 180° common phase rotation was applied to $\mathbf{z}_1$ to obtain $\mathbf{z}_2$. In order to convert a 4D real vector to a Stokes vector, first, the Jones vector should be obtained by reversing the operation in (3.23), and then the Stokes vector can be obtained by (3.36).

The Stokes vectors are optically observable quantities proportional to the squared field, and are often represented as points on a sphere, called the *Poincaré sphere*. The Poincaré sphere offers a good visual representation of the SOPs, where each SOP represents a point on this sphere and the drift of the SOP can be visualized as a rotation of the sphere. Fig. 3.2 illustrates PM-QPSK in the Jones/4D real space and in the Stokes space (plotted on the Poincaré sphere). In the former case, the constellation has four points in each polarization, thus resulting in a total of 16 points (all possible combinations between the two polarizations). On the other hand, in the Stokes space, the constellation has only four points since this representation is invariant to common phase shifts.

The analogous Stokes propagation model of (3.17) or (3.24) models only the SOP drift without the phase noise and can be written as

$$\mathbf{s}_{\mathbf{r}_k} = \mathbf{M}_k \mathbf{s}_{\mathbf{u}_k} + \mathbf{s}_{\mathbf{n}_k}, \tag{3.37}$$

where $\mathbf{s}_{\mathbf{u}_k}$ ($\mathbf{s}_{\mathbf{r}_k}$) is the transmitted (received) Stokes vector and can be obtained by applying (3.36) to $\mathbf{u}_k$ ($\mathbf{r}_k$) and $\mathbf{s}_{\mathbf{n}_k}$ is the noise term. The matrix $\mathbf{M}_k$ is a 3×3 real orthogonal matrix, called *Mueller matrix*, which models only the SOP drift equivalently to $\mathbf{J}_k$ in (3.17) such that

$$\mathbf{s}_{\mathbf{J}_k \mathbf{u}_k} = \mathbf{s}_{\mathbf{H}_k \mathbf{u}_k} = \mathbf{M}_k \mathbf{s}_{\mathbf{u}_k}, \tag{3.38}$$

where $\mathbf{s}_{\mathbf{J}_k \mathbf{u}_k}$ ($\mathbf{s}_{\mathbf{H}_k \mathbf{u}_k}$) is obtained by applying (3.36) to $\mathbf{J}_k \mathbf{u}_k$ ($\mathbf{H}_k \mathbf{u}_k$). The noise component $\mathbf{s}_{\mathbf{n}_k}$ consists of three terms and cannot be obtained by (3.36). It can be identified

by equating terms in two expressions for $\mathbf{s}_{\mathbf{r}_k}$, where one is obtained by applying (3.36) to both sides of (3.5) and applying (3.38), and the other is (3.37). Thus,

$$\mathbf{s}_{\mathbf{n}_k} = (\mathbf{H}_k\mathbf{u}_k)^{\mathrm{H}}\vec{\boldsymbol{\sigma}}\mathbf{n}_k + \mathbf{n}_k^{\mathrm{H}}\vec{\boldsymbol{\sigma}}\mathbf{H}_k\mathbf{u}_k + \mathbf{n}_k^{\mathrm{H}}\vec{\boldsymbol{\sigma}}\mathbf{n}_k, \tag{3.39}$$

$$= (e^{-i\phi_k}\mathbf{J}_k\mathbf{u}_k)^{\mathrm{H}}\vec{\boldsymbol{\sigma}}\mathbf{n}_k + \mathbf{n}_k^{\mathrm{H}}\vec{\boldsymbol{\sigma}}e^{-i\phi_k}\mathbf{J}_k\mathbf{u}_k + \mathbf{n}_k^{\mathrm{H}}\vec{\boldsymbol{\sigma}}\mathbf{n}_k, \tag{3.40}$$

where the first two terms represent the signal–noise interaction and the last one the noise–noise interaction. As can be noted, $\mathbf{s}_{\mathbf{n}_k}$ is signal-dependent and (3.37) is not an additive-noise model, opposed to (3.5), (3.17), and (3.24).

The matrix $\mathbf{M}_k$ belongs to the special orthogonal group of 3×3 matrices $SO(3)$ satisfying

$$\mathbf{M}_k^{\mathrm{T}}\mathbf{M}_k = \mathbf{M}_k\mathbf{M}_k^{\mathrm{T}} = \mathbf{I}_3, \tag{3.41}$$

$$\det \mathbf{M}_k = 1, \tag{3.42}$$

and the polarization transformation modeled by it can be seen as a rotation of the Poincaré sphere. A generic 3×3 real matrix has nine DOFs, whereas after constraining $\mathbf{M}_k$ to fulfill (3.41)–(3.42), it can be shown that it has only three DOFs. Such matrices can be expressed using the matrix function [41]

$$M(\boldsymbol{\alpha}) = \exp(2\mathcal{K}(\boldsymbol{\alpha})) = \exp(2\theta\mathcal{K}(\mathbf{a})), \tag{3.43}$$

$$= \mathbf{I}_3 + \sin(2\theta)\mathcal{K}(\mathbf{a}) + (1 - \cos(2\theta))\mathcal{K}(\mathbf{a})^2, \tag{3.44}$$

where

$$\mathcal{K}(\mathbf{a}) = \begin{pmatrix} 0 & -a_3 & a_2 \\ a_3 & 0 & -a_1 \\ -a_2 & a_1 & 0 \end{pmatrix}. \tag{3.45}$$

The transformation in (3.43) can be viewed in the axis-angle rotation description as a rotation around the unit vector $\mathbf{a}$ by an angle 2θ. The inverse of $M(\boldsymbol{\alpha})$ can be obtained by

$$M(\boldsymbol{\alpha})^{-1} = M(\boldsymbol{\alpha})^{\mathrm{T}} = M(-\boldsymbol{\alpha}). \tag{3.46}$$

3.2 Phase Noise

The phase noise in (3.5), (3.17), or (3.24) is modeled as a Wiener process [35, 48]

$$\phi_k = \dot{\phi}_k + \phi_{k-1}, \tag{3.47}$$

where $\dot{\phi}_k$ is the *innovation* of the phase noise. The innovation $\dot{\phi}_k$ is a real Gaussian random variable drawn independently at each time instance k

$$\dot{\phi}_k \sim \mathcal{N}(0, \sigma_\nu^2), \tag{3.48}$$

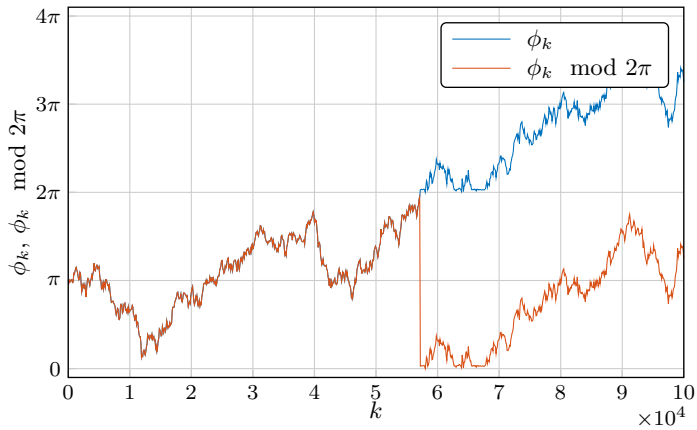

Figure 3.3: An example of phase noise random walk for $\sigma_\nu^2 = 2.25 \cdot 10^{-4}$.

where the variance $\sigma_\nu^2 = 2\pi\Delta\nu T$, and $\Delta\nu$ is the sum of the linewidths of the transmitter and receiver lasers.

The acquired phase noise at time k is the summation of the innovations $\dot{\phi}_1, \ldots, \dot{\phi}_k$ and the initial phase ϕ_0. Since the $\dot{\phi}_1, \ldots, \dot{\phi}_k$ terms are Gaussian, ϕ_k becomes a Gaussian-distributed random variable with mean ϕ_0 and variance $k\sigma_\nu^2$. Due to the periodicity with period 2π of the function $e^{-i\phi_k}$, the phase angle ϕ_k can be bounded to the interval $[0, 2\pi)$ by applying the modulo 2π operation. In this case, the probability density function (pdf) of ϕ_k becomes a wrapped (around the unit circle) Gaussian distribution. Fig. 3.3 shows an example of a phase noise random walk and the corresponding wrapped phase noise. The evolution of the wrapped phase noise pdf is shown in [Paper A, Fig. 1]. The initial phase difference ϕ_0 between the two free running lasers has equal probability for every value, therefore it is common to model ϕ_0 as a random variable uniformly distributed in the interval $[0, 2\pi)$.

3.3 Polarization State Drift

As mentioned in Section 2.1.3, the SOP of the received signal will be different from the one at the transmitter due to various imperfections of the fiber cable. This transformation between the input and output SOPs is a dynamic process that changes over time irrespectively of the input SOP. Plotting the Stokes vectors on the Poincaré sphere is often used as a good visual representation of the phenomenon.

Fig. 3.4 illustrates the trajectory of the received Stokes vectors for a fixed input over time. The plotted data was obtained by measuring a 127 km long buried fiber for 36 days at every ~ 2.2 h (shown by the dots in the figure). The technicalities of the measurement setup and postprocessing have been published elsewhere [49]. As can be seen, the SOP

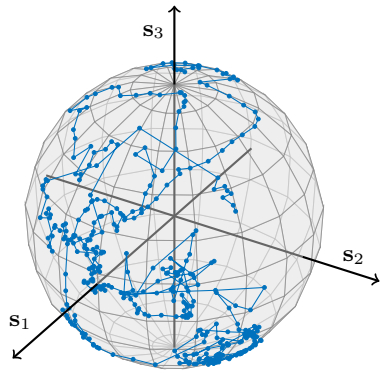

Figure 3.4: The trajectory of a measured SOP drift is plotted. Each dot represents a measurement taken ~ 2.2 h apart.

has a random behavior, taking steps of various sizes in no preferred direction.

Several variations of polarization drift models have been proposed and used in the literature, most commonly in the context of equalization design. These models can be distinguished by the dynamism and randomness of their behavior in time. In the next sections, different variations will be reviewed.

3.3.1 Static

The simplest and most straightforward solution is to generate a Jones/Mueller/4D matrix randomly, which thereafter is kept constant [50–53]. This assumption is reasonable if the considered time scale is small compared to time scale of the SOP drift. As can be seen in Fig. 3.4, the SOP does not change significantly between two consecutive measurements taken ~ 2.2 h apart. Therefore, if, e.g., 10^4 symbols at 28 Gbaud are considered, these correspond to 0.35 µs, which is a too short time to have significant changes of the SOP. Of course this depends on the installation specifics of the fiber. Aerial fibers will change at a much faster pace than the more stable buried fibers.

The Jones/Mueller/4D matrix can be generated using several approaches by either choosing $\boldsymbol{\alpha}$ and ϕ according to a certain pdf or randomly selecting the elements of the matrix. The latter approach does not certify unitarity/orthogonality of the matrices, and therefore it must be followed by a normalization process. Different approaches will sample the space of possible unitary/orthogonal matrices according to different distributions. In [54], a method to generate $\boldsymbol{\alpha}$ is described such that the space of all possible Mueller matrices is uniformly sampled. In this case, all the possible SOP are equally likely after applying such a matrix to a constant Stokes vector. The same method to generate $\boldsymbol{\alpha}$ can be used to form Jones (3.15) or 4D matrices (3.28), where in addition ϕ should be selected uniformly in the interval $[0, 2\pi)$ in order to obtain a uniform sampling of all possible $\mathbf{H}_k$ and $\mathbf{R}_k$.

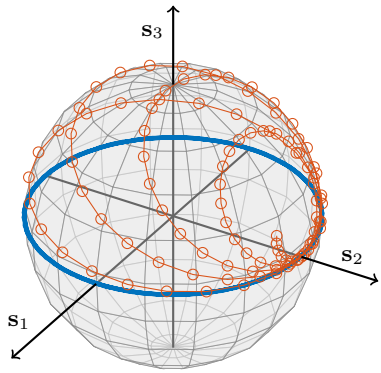

Figure 3.5: SOP trajectories obtained by modeling $\alpha_3 = \omega T k$ (blue curve in the $\mathbf{s}_1$-$\mathbf{s}_2$ plane), and $\alpha_2 = \omega_1 T k$ and $\alpha_3 = \omega_2 T k$ (red curve with round markers).

3.3.2 Dynamic Deterministic

Another option to emulate SOP drift is to model the elements of $\boldsymbol{\alpha}$ as frequency components. For example, in [31, 55, 56], SOP drift was simulated by modeling $\alpha_3 = \omega T k$ and setting $\alpha_1 = \alpha_2 = 0$. Another practice is to only set $\alpha_1 = 0$ and vary α_2 and α_3 at different frequencies, i.e., $\alpha_2 = \omega_1 T k$ and $\alpha_3 = \omega_2 T k$ [23, 57, 58].

Fig. 3.5 illustrates the trajectories obtained by the methods described above. As can be seen, these methods have a cyclic/quasi-cyclic deterministic behavior and cover all possible SOPs on the Poincaré sphere in a nonuniform pattern.

3.3.3 Dynamic Stochastic

As can be seen in Fig. 3.4, the SOP has a random trajectory and cannot be accurately modeled with a deterministic behavior such as those discussed in the previous section and shown in Fig. 3.5. A attempt to emulate stochastic polarization drifts for the first time in the polarization literature was made in our prestudy [59] for Paper A. In [59], we modeled[3] $\mathbf{M}_k$ in (3.37) as

$$\mathbf{M}_k = M(\boldsymbol{\alpha}_k), \tag{3.49}$$

where $\boldsymbol{\alpha}_k$ follows, analogously to the phase noise, a Wiener process

$$\boldsymbol{\alpha}_k = \dot{\boldsymbol{\alpha}}_k + \boldsymbol{\alpha}_{k-1}, \tag{3.50}$$

and $\dot{\boldsymbol{\alpha}}_k$ is the *innovation* of the SOP drift, cf. (3.47). The innovation parameters are random and drawn independently from a zero-mean real Gaussian distribution at each time instance k

$$\dot{\boldsymbol{\alpha}}_k \sim \mathcal{N}(\mathbf{0}, \sigma_p^2 \, \mathbf{I}_3), \tag{3.51}$$

[3] The model proposed in [59] is described here in the Stokes space. However, the same model applies to the other two descriptions as well.

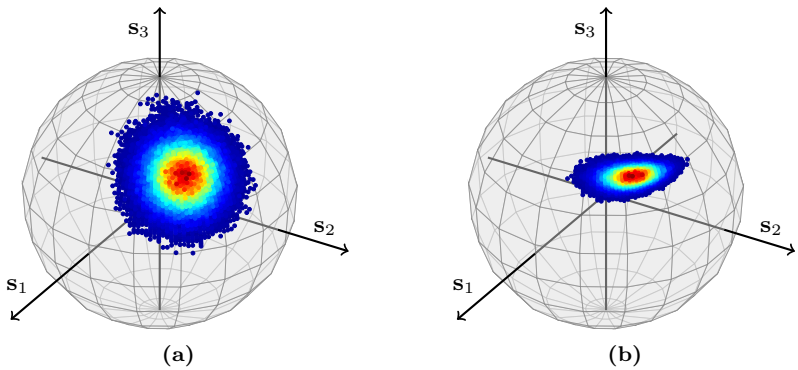

Figure 3.6: The histograms of $M(\dot{\boldsymbol{\alpha}}_k + \boldsymbol{\alpha}_{k-1})\mathbf{s}_{\mathbf{u}_k}$ for different $\boldsymbol{\alpha}_{k-1}$ and a fixed $\mathbf{s}_{\mathbf{u}_k}$ are shown. The highest density is represented by dark red and the lowest by dark blue, the outer part of the histogram. The figure on the left (a) was obtained for $\boldsymbol{\alpha}_{k-1} = [0, 0, 0]^{\mathrm{T}}$, whereas the figure on the right (b) was obtained for $\boldsymbol{\alpha}_{k-1} = [0, 0, 2\pi/4]^{\mathrm{T}}$. In both cases $\sigma_p^2 = 0.007$.

where $\sigma_p^2 = 2\pi\Delta p\, T$. We refer to Δp as the *polarization linewidth*, which quantifies the speed of the SOP drift, analogous to the linewidth describing the phase noise, cf. (3.48).

However, this model is not a stationary random process, as the pdf of $M(\boldsymbol{\alpha}_k)$ depends not only on $\dot{\boldsymbol{\alpha}}_k$ in (3.50), but on $\boldsymbol{\alpha}_{k-1}$ as well, which is nonstationary. Therefore the statistics of $M(\boldsymbol{\alpha}_k)$ vary with $\boldsymbol{\alpha}_{k-1}$ and time k. On the contrary, the statistics of a stationary random process should depend only on the innovation $\dot{\boldsymbol{\alpha}}_k$. A (visual) comparison between two histograms of $\mathbf{M}_k\mathbf{s}_{\mathbf{u}_k}$ obtained for different $\boldsymbol{\alpha}_{k-1}$ but same σ_p^2 and $\mathbf{s}_{\mathbf{u}_k}$ is shown in Fig. 3.6. As can be seen, the shape of the histograms is different and confirm the nonstationary property of the random process $\mathbf{M}_k\mathbf{s}_{\mathbf{u}_k}$. Moreover, for $\boldsymbol{\alpha}_{k-1} = [0, 0, 3\pi/4]^{\mathrm{T}}$ (b), in contrast with the other case $\boldsymbol{\alpha}_{k-1} = [0, 0, 0]^{\mathrm{T}}$ (a), the histogram is not isotropic, and by isotropic we mean that all the possible orientations of the changes of the Stokes vector are equally likely.

In conclusion, this model is neither stationary nor isotropic. Our goal in Paper A is to find a model that satisfies both conditions. The main difference between the model in [59] and the one in Paper A consists in the updating method of the matrix $\mathbf{M}_k$, which is done as a multiplication of matrices [Paper A, eq. (A.15)]

$$\mathbf{M}_k = M(\dot{\boldsymbol{\alpha}}_k)\mathbf{M}_{k-1}, \tag{3.52}$$

where $\dot{\boldsymbol{\alpha}}_k$ is modeled as (3.51). This model has been experimentally validated and its details together with the analogue Jones and 4D descriptions can be found in Paper A.

CHAPTER 4

Phase and Polarization Tracking Algorithms

In the present chapter are discussed estimation and compensation algorithms of the phase noise and SOP drift presented in Chapter 3. First, an algorithm for phase tracking is described in Section 4.1. Thereafter, in Section 4.2, an SOP recovery algorithm for PM-QPSK is presented, and then the generalized version of the algorithm, to account for PM-QAM, is described in Section 4.3. In Section 4.4, a tracking algorithm that accounts jointly for both considered impairments is presented. This chapter reviews the required background knowledge required for Paper B, wherein we propose a tracking algorithm (summarized in Section 4.5) that jointly recovers the phase and the SOP.

4.1 Blind Phase Search Algorithm

The blind phase search (BPS) algorithm estimates the phase noise ϕ_k and compensates for it in a feedforward fashion in each polarization separately[1] [35].

Assuming that the received signal is sampled at the symbol rate and it is only affected by phase noise and additive noise, the received symbols can be modeled as a special case of (3.17)

$$\mathbf{r}_k = e^{-i\phi_k}\mathbf{u}_k + \mathbf{n}_k, \tag{4.1}$$

and can seen in Fig. 2.3.

The BPS algorithm for QAM constellations can be summarized by the following steps:

[1] It is possible to phase track jointly the two polarizations. However, in this case, the relative phase offset between the two polarization must be compensated in advance.

1. The received signal is rotated by P_{BPS} test phases

$$z_{k,b} = r_k e^{i\phi_b}, \tag{4.2}$$

where r_k is one element of $\mathbf{r}_k$ and

$$\phi_b = \frac{b}{P_{\mathrm{BPS}}} \cdot \frac{\pi}{2}, \text{ for } b = 0, \ldots, P_{\mathrm{BPS}} - 1. \tag{4.3}$$

Note that the range of ϕ_b is $[0, \pi/2]$ due to the $\pi/2$ rotational symmetry of QAM constellations. For other constellations, this range must be adjusted accordingly.

2. The rotated symbols $z_{k,b}$ are fed into a decision circuit to calculate the squared Euclidean distance to the closest constellation point

$$d_{k,b}{}^2 = |z_{k,b} - \hat{z}_{k,b}|^2, \tag{4.4}$$

where $\hat{z}_{k,b}$ is the point of the constellation whose position is the closest to $z_{k,b}$.

3. The impact of the additive noise $\mathbf{n}_k$ is reduced by a moving sum over $2N_{\mathrm{BPS}} + 1$ previously calculated distances

$$s_{k,b} = \sum_{n=-N_{\mathrm{BPS}}}^{N_{\mathrm{BPS}}} d_{k-n,b}{}^2. \tag{4.5}$$

4. The optimal phase angle is determined by the minimum sum of distances, and the decoded symbol can be selected from $\hat{\mathbf{z}}_{k,b}$ based on the index b of the minimum sum $s_{k,b}$.

The $\pi/2$ symmetry of QAM constellations leads to a four-fold ambiguity. For example, if the phase noise passes to the second quadrant, say, $\phi_k = 3\pi/4$, the algorithm will misinterpret the phase angle as being in the first quadrant $\phi_k - \pi/2$. This will lead to catastrophic errors and can be avoided using differential coding [24, Sec. 2.6.1]. Moreover, the calculated phase angles by the algorithm are in the interval $[0, \pi/2]$, but the phase evolves and extends over this interval leading to a performance penalty. Therefore, to account for this event, a phase unwrapper is needed [60], thus introducing feedback in the algorithm. The purpose of the phase unwrapper, in this case, is to add multiples of $\pi/2$ to the estimated phase such that the maximum phase difference between two adjacent phase estimates is less than $\pi/4$.

4.2 Constant Modulus Algorithm

The CMA was initially developed for two-dimensional QPSK signals [61] and then applied to 4D PM-QPSK optical constellations to recover the SOP [23]. The considered signal model is

$$\mathbf{r}_k = \mathbf{J}_k \mathbf{u}_k + \mathbf{n}_k, \tag{4.6}$$

obtained by neglecting the phase noise in (3.17).

The CMA reverses the channel effects using a previous estimate of $\mathbf{J}_k$

$$\mathbf{r}'_k = \hat{\mathbf{J}}_{k-1}\mathbf{r}_k, \tag{4.7}$$

which can be expanded into

$$\begin{pmatrix} r'_{x,k} \\ r'_{y,k} \end{pmatrix} = \begin{pmatrix} \hat{J}_{xx,k-1} & \hat{J}_{xy,k-1} \\ \hat{J}_{yx,k-1} & \hat{J}_{yy,k-1} \end{pmatrix} \begin{pmatrix} r_{x,k} \\ r_{y,k} \end{pmatrix}. \tag{4.8}$$

The purpose of the CMA is to minimize the magnitude of the error functions

$$\epsilon_x = \left|r'_{x,k}\right|^2 - E_s, \tag{4.9}$$

$$\epsilon_y = \left|r'_{y,k}\right|^2 - E_s, \tag{4.10}$$

which minimize the distance of the algorithm's output $r'_{x/y,k}$ to the circle of radius equal to the QPSK symbol energy. The update of $\hat{\mathbf{J}}_{k-1}$ is often done using the gradient descent method [62, p. 466] resulting in the update rules

$$\hat{J}_{xx,k} = \hat{J}_{xx,k-1} - \mu_{\text{CMA}}\epsilon_x r'_{x,k}(r_{x,k})^*, \tag{4.11}$$

$$\hat{J}_{xy,k} = \hat{J}_{xy,k-1} - \mu_{\text{CMA}}\epsilon_x r'_{x,k}(r_{y,k})^*, \tag{4.12}$$

$$\hat{J}_{yx,k} = \hat{J}_{yx,k-1} - \mu_{\text{CMA}}\epsilon_y r'_{y,k}(r_{x,k})^*, \tag{4.13}$$

$$\hat{J}_{yy,k} = \hat{J}_{yy,k-1} - \mu_{\text{CMA}}\epsilon_y r'_{y,k}(r_{y,k})^*, \tag{4.14}$$

where μ_{CMA} is a positive tracking step size parameter.

As suggested by its name, the algorithm was designed for constellations with constant modulus, such as phase-shift keying. Applying the algorithm to constellations with multiple modulus, such as 16-QAM, degrades the performance significantly. However, the CMA has been extended to multiple-modulus constellations and it is presented in the next section.

4.3 Multiple Modulus Algorithm

The MMA is based on the same principle as the CMA discussed earlier, except that the error function is calculated between the algorithm's output and the nearest constellation radius [63]. Due to the radius-directed error, the algorithm is known in the literature also as the radius-directed algorithm/equalizer [64].

The MMA makes first a decision on the constellation ring to which the received symbol most likely belongs, and then adapts $\hat{\mathbf{J}}_{k-1}$ such that this distance is minimized using the same updating rules as the CMA (4.11)–(4.14). The modified error functions (4.9)–(4.10) are

$$\epsilon_x = \left|r'_{x,k}\right|^2 - a^2_{x,k}, \tag{4.15}$$

$$\epsilon_y = \left|r'_{y,k}\right|^2 - a^2_{y,k}, \tag{4.16}$$

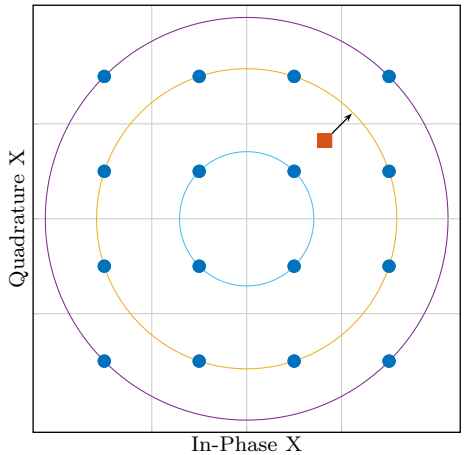

Figure 4.1: The principle of MMA illustrated for 16-QAM. The algorithm updates $\hat{\mathbf{J}}_{k-1}$ such that the error between the received symbol (red square) and its nearest constellation ring is minimized.

where $a_{x,k}$ ($a_{y,k}$) is the nearest radius to $r'_{x,k}$ ($r'_{y,k}$). It should be noted that the CMA is a special case of the MMA applied to a one-ring constellation. Fig. 4.1 shows an example of the algorithm's principle. In this example, only the X polarization is shown, however, the same operation is carried out in the Y polarization.

As can be seen in (4.9)–(4.10) and (4.15)–(4.16), the error functions of both the CMA and MMA are immune to the phase of the received signal. Therefore, the algorithms are not affected by phase variations and can be applied before phase compensation (Section 4.1). However, an extra phase shift may be inserted when updating $\hat{\mathbf{J}}_k$ in (4.11)–(4.14). Compared to the laser phase noise, the drift of this phase shift is slow, but it can introduce a relative phase offset between the two polarizations, which must be tracked for 4D constellations.

The CMA and MMA stated above are presented as single-tap equalizers. In other words, the estimate of the channel matrix $\hat{\mathbf{J}}_k$ is a single matrix. However, this is not the case in practice, where $\hat{\mathbf{J}}_k$ is a bank of four finite-impulse response filters. In this case, the elements of $\hat{\mathbf{J}}_k$ and $\mathbf{r}_k$, i.e., $\hat{J}_{xx,k}, \hat{J}_{xy,k}, \hat{J}_{yx,k}, \hat{J}_{yy,k}, r_{x,k}$, and $r_{y,k}$, become vectors and $\mathbf{r}'_k$ is calculated in (4.7) as a weighted sum of a block of rotated received symbols $\mathbf{r}_k$. By extending the algorithms to the multi-tap version, it is possible to perform, besides polarization tracking, adaptive-channel equalization such as PMD compensation, residual-dispersion compensation, intersymbol-interference mitigation, and approximate a matched filter.

4.4 Kabsch Algorithm

The Kabsch algorithm [57] addresses jointly the phase and SOP tracking by estimating $\mathbf{R}_k$ in the 4D space (Section 3.1.2). The tracking is carried out over blocks of N_{Kab} PM symbols

$$\mathbf{V}_{\mathbf{u}_l} = [\mathbf{v}_{\mathbf{u}_k}, \mathbf{v}_{\mathbf{u}_{k+1}}, \ldots, \mathbf{v}_{\mathbf{u}_{k+N_{\text{Kab}}-1}}], \tag{4.17}$$

under the assumption that $\mathbf{R}_k$ does not change (significantly) over the block l.

The algorithm can be summarized by the following steps:

1. The received block of symbols $\mathbf{V}_{\mathbf{r}_l}$ is derotated using the inverse of a previous estimate of $\mathbf{R}_l$
$$\mathbf{V}'_{\mathbf{r}_l} = \hat{\mathbf{R}}_{l-1}^{-1} \mathbf{V}_{\mathbf{r}_l}. \tag{4.18}$$

2. The estimated transmitted block of symbols $\mathbf{V}_{\hat{\mathbf{u}}_l}$ is obtained by the minimum Euclidean distance between $\mathbf{V}'_{\mathbf{r}_l}$ and the constellation points.

3. The matrix $\hat{\mathbf{R}}_l$ is updated as
$$\hat{\mathbf{R}}_l = \mathbf{U}_l \begin{pmatrix} 1 & 0 & 0 & 0 \\ 0 & 1 & 0 & 0 \\ 0 & 0 & 1 & 0 \\ 0 & 0 & 0 & s \end{pmatrix} \mathbf{W}_l^{\mathrm{T}}, \tag{4.19}$$
where $s = \text{sign}(\det(\mathbf{U}_l \mathbf{W}_l^{\mathrm{T}}))$, and $\mathbf{U}_l$ and $\mathbf{W}_l$ are the left- and right-singular vectors of $\mathbf{C}_l = \mathbf{V}_{\hat{\mathbf{u}}_l} \times \mathbf{V}_{\mathbf{r}_l}^{\mathrm{T}}$, i.e., $\mathbf{U}_l \Sigma_l \mathbf{W}_l^{\mathrm{T}} = \mathbf{C}_l$ is the singular-value decomposition [65, p. 35] of $\mathbf{C}_l$.

The Kabsch algorithm can be applied to arbitrary constellations by only changing the decision stage in step 2. This algorithm, as the BPS, suffers from ambiguities, and therefore differential coding must be applied to ensure reliability.

4.5 Proposed Algorithm

The proposed algorithm in Paper B recovers the carrier phase and SOP for arbitrary modulation formats using a non-data aided decision-directed architecture. Similarly to the Kabsch algorithm, the proposed algorithm operates jointly on both polarizations, but in a symbol-by-symbol fashion without averaging blocks. The algorithm has been developed based on the channel model proposed in Paper A and is the first model-based SOP tracking algorithm. Model-based algorithms have a restricted flexibility and therefore fewer DOFs to adjust resulting in a more efficient impairment cancellation, rather than scanning over a larger domain in order to find the optimal setup. At similar

or better performance, the proposed algorithm offers a good trade-off between complexity and performance compared to state-of-the-art algorithms regardless of the modulation format. The details of the algorithm can be found in Paper B.

CHAPTER 5

Contributions

This chapter summarizes the contributions of the appended papers.

Paper A

"**Polarization Drift Channel Model for Coherent Fibre-Optic Systems**"

In this paper, we propose a theoretical framework to model the dynamical changes of the SOP in coherent fiber-optic systems, based on a generalization of the one-dimensional phase-noise random walk to higher dimensions, accounting for the random polarization drift. The model is stated in the Jones, Stokes, and real 4D formalisms and can be easily combined with other transmission impairments to form a complete channel model. The proposed polarization drift model is the first of its kind and will likely be useful in many areas of photonics where stochastic polarization fluctuation is an issue. Based on this model, better polarization tracking algorithms can be found and more accurate simulations that reflect fiber behavior closely can be performed in order to quantify system performance.

Contributions: CBC designed and analyzed the model, carried out simulations, and wrote the paper. MK and EA formulated the problem and contributed to the analysis. PJ provided mathematical expertise and interpretation of the results. All authors reviewed and revised the paper.

Paper B

"**Modulation Format Independent Joint Polarization and Phase Tracking for Coherent Receivers**"

Based on the model proposed in Paper A, we propose an algorithm to recover jointly the carrier phase and SOP for arbitrary modulation formats. The algorithm uses a non-data aided, decision-directed architecture, hence zero overhead, and operates jointly on both polarizations. The performance and complexity of the algorithm is investigated by comparing it with state-of-the-art algorithms for different modulation formats. The proposed algorithm performs similarly or better than state-of-the-art algorithms presented in Sections 4.1–4.4 and provides a good trade-off between complexity and performance regardless of the modulation format. High performance and fast convergence rate, for any modulation format at low complexity, make the algorithm a strong candidate for future elastic optical systems, where the modulation format can be changed dynamically during transmission to accommodate for various channel and network conditions.

Contributions: CBC analyzed the algorithm, carried out simulations, and wrote the paper. EA proposed the algorithm and contributed to the analysis. MK and PJ provided mathematical expertise and interpretation of the results. All authors reviewed and revised the paper.

Bibliography

[1] R. W. Tkach, "Scaling optical communications for the next decade and beyond," *Bell Labs Technical Journal*, vol. 14, no. 4, pp. 3–10, Feb. 2010.

[2] S. Abbott, "Review of 20 years of undersea optical fiber transmission system development and deployment since TAT-8," in *Proc. European Conference on Optical Communication (ECOC)*, Brussels, Belgium, Sept. 2008, p. Mo.4.E.1.

[3] R. Mears, L. Reekie, I. Jauncey, and D. Payne, "Low-noise erbium-doped fibre amplifier operating at 1.54 μm," *Electronics Letters*, vol. 23, no. 19, pp. 1026–1028, Sept. 1987.

[4] E. Desurvire, J. R. Simpson, and P. C. Becker, "High-gain erbium-doped traveling-wave fiber amplifier," *Optics Letters*, vol. 12, no. 11, pp. 888–890, Nov. 1987.

[5] H. Sun, K.-T. Wu, and K. Roberts, "Real-time measurements of a 40 Gb/s coherent system," *Optics Express*, vol. 16, no. 2, pp. 873–879, Jan. 2008.

[6] E. Agrell and M. Karlsson, "Power-efficient modulation formats in coherent transmission systems," *Journal of Lightwave Technology*, vol. 27, no. 22, pp. 5115–5126, Nov. 2009.

[7] G. P. Agrawal, *Fiber-Optic Communication Systems*, 4th ed. Hoboken, NJ: John Wiley & Sons, 2010.

[8] T. Miya, Y. Terunuma, T. Hosaka, and T. Miyashita, "Ultimate low-loss single-mode fibre at 1.55 μm," *Electronics Letters*, vol. 15, no. 4, pp. 106–108, Feb. 1979.

[9] M. N. Islam, "Raman amplifiers for telecommunications," *IEEE Journal of Selected Topics in Quantum Electronics*, vol. 8, no. 3, pp. 548–559, May 2002.

[10] E. Ip, A. P. T. Lau, D. J. F. Barros, and J. M. Kahn, "Coherent detection in optical fiber systems," *Optics Express*, vol. 16, no. 2, pp. 753–791, Jan. 2008.

[11] F. Derr, "Coherent optical QPSK intradyne system: concept and digital receiver realization," *Journal of Lightwave Technology*, vol. 10, no. 9, pp. 1290–1296, Sept. 1992.

[12] D. E. Crivelli, M. R. Hueda, H. S. Carrer, M. del Barco, R. R. López, P. Gianni, J. Finochietto, N. Swenson, P. Voois, and O. E. Agazzi, "Architecture of a single-chip 50 Gb/s DP-QPSK/BPSK transceiver with electronic dispersion compensation for coherent optical channels," *IEEE Transactions on Circuits and Systems I: Regular Papers*, vol. 61, no. 4, pp. 1012–1025, Apr. 2014.

[13] K. Petermann, *Laser Diode Modulation and Noise*. Dordrecht, The Netherlands: Kluwer Academic Publishers, 1988.

[14] G. P. Agrawal, *Nonlinear Fiber Optics*, 4th ed. Burlington, MA: Academic Press, 2007.

[15] R. Kashyap, *Fiber Bragg Gratings*. San Diego, CA: Academic Press, 1999.

[16] S. J. Savory, G. Gavioli, R. I. Killey, and P. Bayvel, "Electronic compensation of chromatic dispersion using a digital coherent receiver," *Optics Express*, vol. 15, no. 5, pp. 2120–2126, Mar. 2007.

[17] H. Kogelnik, R. M. Jopson, and L. E. Nelson, "Polarization-mode dispersion," in *Optical Fiber Telecommunications IV-B: Systems and Impairments*, I. Kaminow and T. Li, Eds. San Diego, CA: Academic Press, 2002, ch. 15, pp. 725–861.

[18] T. Pfau, S. Hoffmann, O. Adamczyk, R. Peveling, V. Herath, M. Porrmann, and R. Noé, "Coherent optical communication: towards realtime systems at 40 Gbit/s and beyond," *Optics Express*, vol. 16, no. 2, pp. 866–872, Jan. 2008.

[19] J. M. Kahn and J. R. Barry, "Wireless infrared communications," *Proceedings of the IEEE*, vol. 85, no. 2, pp. 265–298, Feb. 1997.

[20] A. Larsson, "Advances in VCSELs for communication and sensing," *IEEE Journal of Selected Topics in Quantum Electronics*, vol. 17, no. 6, pp. 1552–1567, Nov.–Dec. 2011.

[21] C. B. Czegledi, M. R. Khanzadi, and E. Agrell, "Bandlimited power-efficient signaling and pulse design for intensity modulation," *IEEE Transactions on Communications*, vol. 62, no. 9, pp. 3274–3284, Sept. 2014.

[22] A. M. Joshi, S. Datta, and A. Crawford, "Next-gen communications fiber: multilevel modulation formats push capacities beyond 100 Gbit/s," *Laser Focus World*, pp. 58–63, Feb. 2012.

[23] S. J. Savory, "Digital coherent optical receivers: algorithms and subsystems," *IEEE Journal of Selected Topics in Quantum Electronics*, vol. 16, no. 5, pp. 1164–1179, Sept.–Oct. 2010.

[24] M. Seimetz, *High-Order Modulation for Optical Fiber Transmission.* Heidelberg, Germany: Springer, 2009.

[25] G. Goldfarb and G. Li, "Chromatic dispersion compensation using digital IIR filtering with coherent detection," *IEEE Photonics Technology Letters*, vol. 19, no. 13, pp. 969–971, Jul. 2007.

[26] A. Sheikh, C. Fougstedt, P. Johannisson, A. Graell i Amat, and P. Larsson-Edefors, "Dispersion compensation filter design optimized for robustness and power efficiency," in *Proc. Signal Processing in Photonic Communication (SPPCom)*, Boston, MA, Jul. 2015, p. SpT3D.2.

[27] C. Fougstedt, A. Sheikh, P. Johannisson, A. Graell i Amat, and P. Larsson-Edefors, "Power-efficient time-domain dispersion compensation using optimized FIR filter implementation," in *Proc. Signal Processing in Photonic Communication (SPPCom)*, Boston, MA, Jul. 2015, p. SpT3D.3.

[28] E. Ip and J. M. Kahn, "Compensation of dispersion and nonlinear impairments using digital backpropagation," *Journal of Lightwave Technology*, vol. 26, no. 20, pp. 3416–3425, Oct. 2008.

[29] N. V. Irukulapati, H. Wymeersch, P. Johannisson, and E. Agrell, "Stochastic digital backpropagation," *IEEE Transactions on Communications*, vol. 62, no. 11, pp. 3956–3968, Nov. 2014.

[30] M. Visintin, G. Bosco, P. Poggiolini, and F. Forghieri, "Adaptive digital equalization in optical coherent receivers with Stokes-space update algorithm," *Journal of Lightwave Technology*, vol. 32, no. 24, pp. 4759–4767, Dec. 2014.

[31] N. J. Muga and A. N. Pinto, "Adaptive 3-D Stokes space-based polarization demultiplexing algorithm," *Journal of Lightwave Technology*, vol. 32, no. 19, pp. 3290–3298, Oct. 2014.

[32] A. Leven, N. Kaneda, U.-V. Koc, and Y.-K. Chen, "Frequency estimation in intradyne reception," *IEEE Photonics Technology Letters*, vol. 19, no. 6, pp. 366–368, Mar. 2007.

[33] M. Selmi, Y. Jaouen, and P. Ciblat, "Accurate digital frequency offset estimator for coherent PolMux QAM transmission systems," in *Proc. European Conference on Optical Communication (ECOC)*, Vienna, Austria, Sept. 2009, p. P3.08.

[34] A. Viterbi and A. Viterbi, "Nonlinear estimation of PSK-modulated carrier phase with application to burst digital transmission," *IEEE Transactions on Information Theory*, vol. 29, no. 4, pp. 543–551, Jul. 1983.

[35] T. Pfau, S. Hoffmann, and R. Noé, "Hardware-efficient coherent digital receiver concept with feedforward carrier recovery for M-QAM constellations," *Journal of Lightwave Technology*, vol. 27, no. 8, pp. 989–999, Apr. 2009.

[36] B. P. Smith and F. R. Kschischang, "Future prospects for FEC in fiber-optic communications," *IEEE Journal of Selected Topics in Quantum Electronics*, vol. 16, no. 5, pp. 1245–1257, Sept. 2010.

[37] L. Schmalen, A. J. de Lind van Wijngaarden, and S. ten Brink, "Forward error correction in optical core and optical access networks," *Bell Labs Technical Journal*, vol. 18, no. 3, pp. 39–66, Dec. 2013.

[38] D. A. Morero, M. A. Castrillón, A. Aguirre, M. R. Hueda, and O. E. Agazzi, "Design trade-offs and challenges in practical coherent optical transceiver implementations," *Journal of Lightwave Technology*, to appear, 2016.

[39] A. Goldsmith, S. A. Jafar, N. Jindal, and S. Vishwanath, "Capacity limits of MIMO channels," *IEEE Journal on Selected Areas in Communications*, vol. 21, no. 5, pp. 684–702, Jun. 2003.

[40] N. J. Frigo, "A generalized geometrical representation of coupled mode theory," *IEEE Journal of Quantum Electronics*, vol. 22, no. 11, pp. 2131–2140, Nov. 1986.

[41] J. P. Gordon and H. Kogelnik, "PMD fundamentals: polarization mode dispersion in optical fibers," *Proceedings of the National Academy of Sciences of the United States of America*, vol. 97, no. 9, pp. 4541–4550, Apr. 2000.

[42] R. Bellman, *Introduction to Matrix Analysis*. New York, NY: McGraw-Hill, 1960.

[43] M. Karlsson, "Four-dimensional rotations in coherent optical communications," *Journal of Lightwave Technology*, vol. 32, no. 6, pp. 1246–1257, Mar. 2014.

[44] S. Betti, F. Curti, G. De Marchis, and E. Iannone, "A novel multilevel coherent optical system: 4-quadrature signaling," *Journal of Lightwave Technology*, vol. 9, no. 4, pp. 514–523, Apr. 1991.

[45] R. Cusani, E. Iannone, A. M. Salonico, and M. Todaro, "An efficient multilevel coherent optical system: M-4Q-QAM," *Journal of Lightwave Technology*, vol. 10, no. 6, pp. 777–786, Jun. 1992.

[46] G. G. Stokes, "On the composition and resolution of streams of polarized light from different sources," *Transactions of the Cambridge Philosophical Society*, vol. 9, pp. 399–416, Jan. 1851.

[47] J. N. Damask, *Polarization Optics in Telecommunications*. New York, NY: Springer, 2005.

[48] M. Tur, B. Moslehi, and J. Goodman, "Theory of laser phase noise in recirculating fiber-optic delay lines," *Journal of Lightwave Technology*, vol. 3, no. 1, pp. 20–31, Feb. 1985.

[49] M. Karlsson, J. Brentel, and P. A. Andrekson, "Long-term measurement of PMD and polarization drift in installed fibers," *Journal of Lightwave Technology*, vol. 18, no. 7, pp. 941–951, Jul. 2000.

[50] K. Kikuchi, "Polarization-demultiplexing algorithm in the digital coherent receiver," in *Digest of the IEEE/LEOS Summer Topical Meetings*, Acapulco, Mexico, Jul. 2008, p. MC22.

[51] L. Liu, Z. Tao, W. Yan, S. Oda, T. Hoshida, and J. C. Rasmussen, "Initial tap setup of constant modulus algorithm for polarization de-multiplexing in optical coherent receivers," in *Proc. Optical Fiber Communication Conference (OFC)*, San Diego, CA, Mar. 2009, p. OMT2.

[52] I. Roudas, A. Vgenis, C. S. Petrou, D. Toumpakaris, J. Hurley, M. Sauer, J. Downie, Y. Mauro, and S. Raghavan, "Optimal polarization demultiplexing for coherent optical communications systems," *Journal of Lightwave Technology*, vol. 28, no. 7, pp. 1121–1134, Apr. 2010.

[53] P. Johannisson, H. Wymeersch, M. Sjödin, A. S. Tan, E. Agrell, P. A. Andrekson, and M. Karlsson, "Convergence comparison of the CMA and ICA for blind polarization demultiplexing," *Journal of Optical Communications and Networking*, vol. 3, no. 6, pp. 493–501, Jun. 2011.

[54] M. Karlsson, C. B. Czegledi, and E. Agrell, "Coherent transmission channels as 4d rotations," in *Proc. Signal Processing in Photonic Communication (SPPCom)*, Boston, MA, Jul. 2015, p. SpM3E.2.

[55] P. Johannisson, M. Sjödin, M. Karlsson, H. Wymeersch, E. Agrell, and P. A. Andrekson, "Modified constant modulus algorithm for polarization-switched QPSK," *Optics Express*, vol. 19, no. 8, pp. 7734–7741, Apr. 2011.

[56] S. J. Savory, "Digital filters for coherent optical receivers," *Optics Express*, vol. 16, no. 2, pp. 804–817, Jan. 2008.

[57] H. Louchet, K. Kuzmin, and A. Richter, "Joint carrier-phase and polarization rotation recovery for arbitrary signal constellations," *IEEE Photonics Technology Letters*, vol. 26, no. 9, pp. 922–924, May 2014.

[58] F. Heismann and K. L. Tokuda, "Polarization-independent electro-optic depolarizer," *Optics Letters*, vol. 20, no. 9, pp. 1008–1010, May 1995.

[59] C. B. Czegledi, E. Agrell, and M. Karlsson, "Symbol-by-symbol joint polarization and phase tracking in coherent receivers," in *Proc. Optical Fiber Communication Conference (OFC)*, Los Angeles, CA, Mar. 2015, p. W1E.3.

[60] E. Ip and J. M. Kahn, "Feedforward carrier recovery for coherent optical communications," *Journal of Lightwave Technology*, vol. 25, no. 9, pp. 2675–2692, Sept. 2007.

[61] D. N. Godard, "Self-recovering equalization and carrier tracking in two-dimensional data communication systems," *IEEE Transactions on Communications*, vol. 28, no. 11, pp. 1867–1875, Nov. 1980.

[62] S. Boyd and L. Vandenberghe, *Convex Optimization*. New York, NY: Cambridge University Press, 2004.

[63] H. Louchet, K. Kuzmin, and A. Richter, "Improved DSP algorithms for coherent 16-QAM transmission," in *Proc. European Conference on Optical Communication (ECOC)*, Brussels, Belgium, Sept. 2008, p. Tu.1.E.6.

[64] M. J. Ready and R. P. Gooch, "Blind equalization based on radius directed adaptation," in *Proc. International Conference on Acoustics, Speech, and Signal Processing (ICASSP)*, Albuquerque, NM, Apr. 1990, pp. 1699–1702.

[65] A. J. Laub, *Matrix Analysis for Scientists & Engineers*. Philadelphia, PA: Society for Industrial and Applied Mathematics, 2005.

CHALMERS UNIVERSITY OF TECHNOLOGY
SE-412 96 Gothenburg, Sweden
Telephone: +46 (0)31 772 10 00
www.chalmers.se